İSTANBUL TECHNICAL UNIVERSITY ★ INSTITUTE OF SCIENCE AND TECHNOLOGY

EXPERIMENTAL INVESTIGATION OF HELICOPTER FUSELAGE AERODYNAMICS

M. Sc. Thesis by

Mehmet Ceylan TOPAL, Aeronautical Eng.

(708011001)

Date of submission : 26 April 2004

Date of defence examination: 20 May 2004

Supervisor (Chairman): Asst. Prof. Dr. Hayri ACAR

Members of the Examining Committee Asst. Prof. Dr. Okşan ÇETİNER-YILDIRIM

Prof. Dr. Erkan AYDER

MAY 2004

İSTANBUL TEKNİK ÜNİVERSİTESİ ★ FEN BİLİMLERİ ENSTİTÜSÜ

HELİKOPTER GÖVDE AERODİNAMİĞİNİN DENEYSEL İNCELENMESİ

YÜKSEK LİSANS TEZİ

Uçak Müh. Mehmet Ceylan TOPAL

(708011001)

Tezin Enstitüye Verildiği Tarih : 26 Nisan 2004
Tezin Savunulduğu Tarih : 20 Mayıs 2004

Tez Danışmanı : **Yrd. Doç. Dr. Hayri ACAR**
Diğer Jüri Üyeleri **Yrd. Doç. Dr. Okşan ÇETİNER-YILDIRIM**
Prof. Dr. Erkan AYDER

Mayıs 2004

FOREWORD

As rotorcrafts have complex aerodynamic structure due to components working close proximity to each other and unsteady characteristics of the flow around the vehicle, it is very difficult to determine the characteristics of complete vehicle. Although there are valuable studies on this subject, there is no complete solution to rotorcraft aerodynamics phenomena. Because of the difficulties in determining complete vehicle characteristics, it is adequate to determine the characteristics components and their effect on the total vehicle performance individually.

In this study we have investigated the isolated fuselage aerodynamic characteristic. Surface flow patterns and flow around fuselage have been investigated. In addition to these aerodynamic coefficients of two different configuration fuselages have been investigated.

Since the rotorcraft experiments are new to ITU Trisonic Research Center, we have modified existing devices and set up new experimental procedures for this purpose. Data acquisition system of Gümüşsuyu wind tunnel balance system created by Ali Levent Hasanreisoğlu has been replaced by new one. I feel obliged to MR. Hasanreisoğlu for his great study on data acquisition system of Gümüşsuyu wind tunnel balance system. It has been a great guide to me when designing the new system.

I owe special thanks to Ass. Prof. Hayri Acar for his support in this study. I especially thanks to Techn. Fikret Özgür and Ali Osman Tabanlı who have played role in achieving this study with their help. I also thanks to all Trisonic Research Center staff and Professors who have provided me this study conditions.

I also feel very grateful to my family and fiancee Bahar Taşan who have never quit supporting me during this study.

April, 2004 Aeronautical Eng. Mehmet Ceylan TOPAL

TABLE OF CONTENTS

NOTATION LIST AND SYMBOLS

α : Angle of incidence

β : Sideslip angle

Σ : Separation or attachment surface

C : Saddle point

C_D : Drag coefficient $\left(\frac{D}{\frac{1}{2}\rho U_\infty^2 S_P}\right)$

C_L : Lift coefficient $\left(\frac{L}{\frac{1}{2}\rho U_\infty^2 S_P}\right)$

C_l : Rolling moment coefficient $\left(\frac{M_X}{\frac{1}{2}\rho U_\infty^2 S_S l}\right)$

C_m : Pitching moment coefficient $\left(\frac{M_Z}{\frac{1}{2}\rho U_\infty^2 S_P l}\right)$

C_n : Yawing moment coefficient $\left(\frac{M_Y}{\frac{1}{2}\rho U_\infty^2 S_S l}\right)$

CTA : Constant Temperature Anemometry

C_Y : Side-force coefficient $\left(\frac{S}{\frac{1}{2}\rho U_\infty^2 S_P}\right)$

D : Drag force

l : Reference length

L : Lifting force

LSB : Least significant bit

LVDT : Linear voltage differential transducer

M_X : Rolling moment

M_Y : Yawing moment

M_Z : Pitching moment

N_D : Droop nose

N_H : Cutback nose

N_S : Symmetrical nose

Re_l : Reynolds number based on reference length. $\left(\frac{\rho U_\infty l}{\mu}\right)$

S : Side-force

S_P : Horizontal projected area

S_S : Side projected area

T_C : Full low cranked tail boom

T_E : High tail boom

T_F : High tail boom

T_H : Straight tail boom

T_L : Full low cranked tail boom

U : Local airspeed

U_∞ : Free stream velocity

LIST OF TABLES

LIST OF FIGURES

HELİKOPTER GÖVDE AERODİNAMİĞİNİN DENEYSEL İNCELEMESİ

ÖZET

Bu çalışmada rüzgar tüneli deneyleri, ITU Trisonik Araştırma Merkezinin tesisleri kullanılarak yapılmıştır. Eiffel ve Gümüşsuyu rüzgar tünelleri bu çalışmada kullanılmıştır.

Helicopter gövdesinin detaylı aerodinamik incelemesi yapılmıştır. Gövde etrafındaki akım niteliksel niceliksel yöntemlerle incelenmiştir. Ayrıca iki farklı gövdeye ait karakteristik aerodinamik katsayılar ve bu katsayıların hücum ve sapma açısıyla nasıl değiştiği deneysel yöntemlerle belirlenmiş, karşılaştırmaları yapılmıştır.

EXPERIMENTAL INVESTIGATION OF HELICOPTER FUSELAGE AERODYNAMICS

SUMMARY

Wind tunnel tests were conducted at the ITU Trisonic Research Center facilities. Eiffel and Gümüşsuyu wind tunnels are used for the experiments.

Detailed investigation of isolated helicopter fuselage aerodynamics has been done for this study. Flow around fuselage has been investigated both qualitatively and quantitatively. For qualitative investigation, oil film and smoke flow with laser visualizations have been done. Velocity magnitudes of flow field around fuselage have been measured by CTA system.

To determine the aerodynamic characteristics of isolated helicopter fuselage of different configurations, balance measurements have been accomplished. The distribution of aerodynamic coefficients with sideslip angle and incidence angle has been investigated. Comparison of two different configuration fuselage shapes has been done.

Results are given after brief explanation of the methods applied, experimental setups and procedures. Images of visualization experiments are given together for different incidence and sideslip angles to be compared. Aerodynamic coefficients are given in graphs together for each configuration to be compared.

1. INTRODUCTION

For many years, wind tunnel testing is a necessity when designing and building a new rotorcraft. Even if we now have more sophisticated codes, more and more detailed experimental results are needed in order to validate these codes and fix their domain of validity. The second reason for wind tunnel testing is to reduce risks and costs in rotorcraft development, especially if we want to use a new design or if we want to fly in a flight domain not yet explored or one that is considered dangerous. "Try before you fly" is perhaps even more necessary for the rotary wing aircraft community then for the fixed wing aircraft community, due to complexity of the configurations involved in aircraft having to assure vertical take-off, hover and forward flight. The third reason for wind tunnel testing is related to the need for optimized configurations. Too many parameters are concerned with this aim and it would be unrealistic to try to build and test too many full-scale prototypes. Wind tunnel testing is a good way to confirm the performance of a specific design and to select the most appropriate configuration to build for flight-testing and validation.

As rotorcrafts being complex flying vehicles, it is more convenient to test the components individually and understand the effects of the components on total vehicle performance. In this study, aerodynamic characteristics of isolated helicopter fuselages of existing designs are investigated to constitute basis for development of new design.

To perform the experiments, suitable techniques of flow visualization are researched and selected for the isolated helicopter fuselage experiments. By the help of new equipment of Trisonic Research Center, adequate experimental setups were obtained for smoke flow visualization with laser sheet.

To determine aerodynamic coefficients of the isolated helicopter fuselage, existing equipment in Gümüşsuyu facilities of the research center was employed. The experiments were achieved using TEM balance system located in this facility. For revising the system, data acquisition setup has been fully changed. Matlab software has been created for calibration and data acquisition of TEM Balance, which will also be useful for preceding studies.

The primary objective of this study is to obtain detailed information about the aerodynamic characteristics of isolated helicopter fuselage. Beside this, the secondary objective is to construct a background, validate the systems and experimental setups for future studies of designing new rotorcraft.

2. HELICOPTER FUSELAGE AERODYNAMICS

There are complex interactional effects between the components of the helicopter configurations due to operation of these components in close proximity to each other.

There exist aerodynamic interactions between main rotor wake and fuselage, main rotor wake and tail rotor wake and also individual rotor blades and their associated wakes.

The dynamics, performance, handling qualities, noise and vibration level of the helicopter configuration may all be influenced by the consequences of the aerodynamic interactions. The severity of the aerodynamic interactions depends mainly on the relative proximity of the individual components. Beside, interactional effects are also functions of flight conditions such as climb, descend, sideward flight and level flight.

These interactional effects have always caused difficulties on the accurate prediction of the aerodynamic characteristics of the rotorcraft configurations. Complex lifting surfaces operating in an unsteady environment present challenge enough, but coupling this flow with the helicopter fuselage shape amplifies the complexity. Often the prediction of isolated rotor aerodynamic is coupled with measured isolated fuselage aerodynamic data or linear fuselage aerodynamics using superposition. But this method is not sufficient to understand the complete phenomena because of the non-linear interaction effects.

Non-linear interaction effects arise in the aerodynamics of the helicopter configurations in some cases. Among these cases, rotor wake affects fuselage onset flow. The presence of the fuselage distorts the rotor wake. This distortion increases as the wake skew angle decreases. (At lower speeds where the wake washes over the body). The influence of the fuselage on the rotor inflow is also significant. Aerodynamics of the rotor blades is changed by the additional inflow distortion due to the presence of the fuselage. This effect changes the strength of the shed wake and contributes to additional distortion of the wake.

According to the difficulties mentioned above, complete analysis and prediction of the aerodynamic characteristics of the helicopter configurations could not have been achieved. There have been number of valuable experimental, numerical and theoretical and investigations on helicopter aerodynamics. These investigations have

been achieved on isolated rotor, isolated fuselage and rotor fuselage combinations and presents basis for the complete analysis and prediction of the aerodynamic characteristics of the helicopter configurations.

In the present study, investigations on isolated fuselage of two different nose and tail configuration model will be done. Balance measurements will be achieved for different values of sideslip angle and angle of incidence of the fuselage. In addition to this, oil film surface flow visualization and smoke flow visualization will be done.

Interactional influences will not be taken into account. The purpose of this study is mainly the prediction of the aerodynamic characteristics of the isolated fuselage.

2.1. Helicopter Fuselage Drag

Helicopter airframe dreg values could be 10 –15 times of those equivalent fixed-wing aircraft. This magnitude of drag is mainly caused by the unavoidable presence of the rotor head above the highest cross sectional area of the fuselage where there's a high super velocity region.

The presence of rotor head causes 30% of the total aircraft drag. Blade folding mechanisms, if employed, increases this value.

The influence of drag on performance can be considerable. Fig 2.1 [1] shows a typical power break down for a helicopter, which shows that the power needed to overcome drag increases rapidly with speed and above 120 kts becomes the largest constituent.

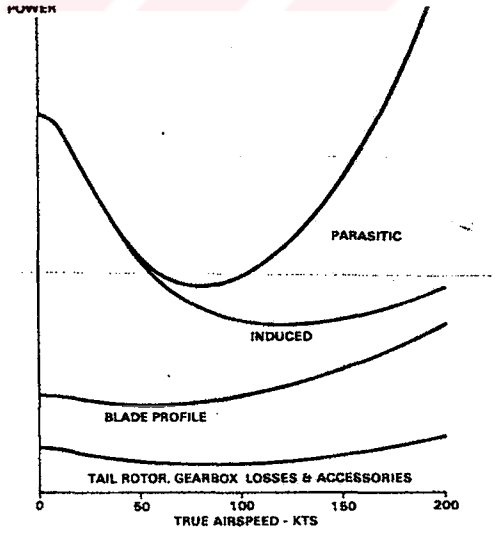

Fig. 2.1 Typical Helicopter Power Breakdown. [1]

Helicopter fuselage shapes can vary according to their operational requirements. In Fig.2.2 [1] typical fuselage configurations are represented. The fuselage has influence on total drag less than 20%, although it is the physically largest component of the helicopter. Fig. 2.3 [4] shows variation of drag coefficients of helicopter components with Reynolds number.

However any drag reduction plan should inevitably start with basic fuselage design before considering the other components.

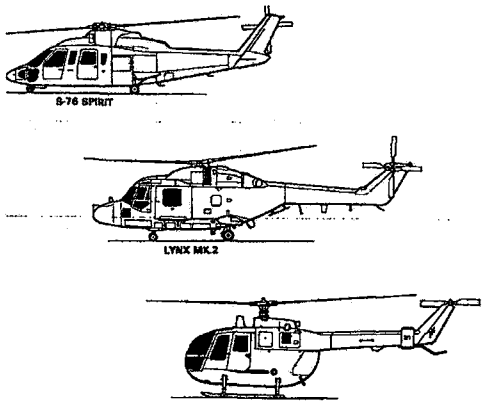

Fig. 2.2 Typical Helicopter Fuselage designs.

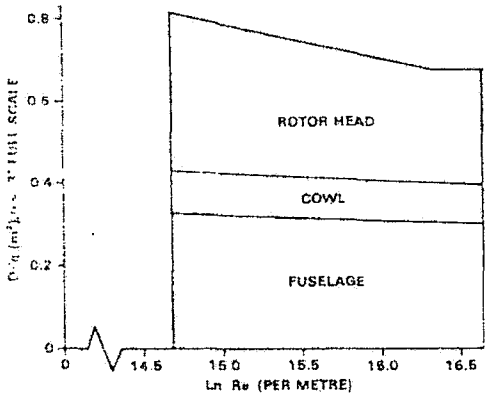

Fig. 2.3 Effect of Reynolds Number on component Drag.

2.1.1. Influence of Fuselage Shape on Drag

For low drag, fuselage cross-section should be circular or near circular. A rectangular cross section increases drag about 50%. Practical nose shapes do not significantly affect the fuselage drag. J.J.Phillipe [4] has shown variation of drag coefficient with angle of incidence for different types of fuselage shapes in Fig.2.4.

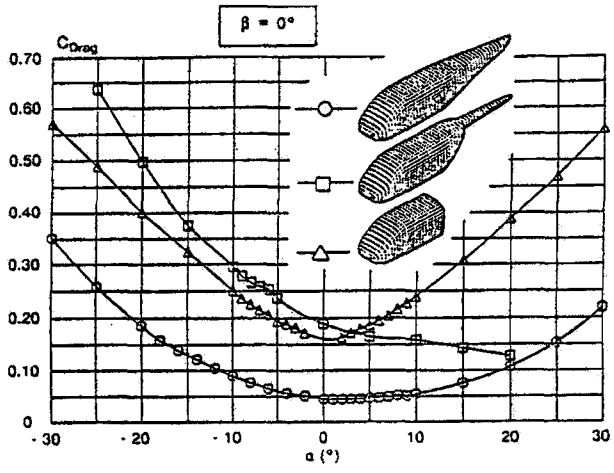

Fig. 2.4 Variation of Drag Coefficient with angle of incidence for 3 different fuselages. [4]

The rear fuselage upsweep has also significant influence on drag. Keys and Wiesner [2] reported 50% increase in CH47 fuselage drag due to negative camber and Seddon

[3] later warned of the danger of fuselage upsweep beyond a critical angle may cause vortex flow that causes large increase in drag in Fig 2.5.

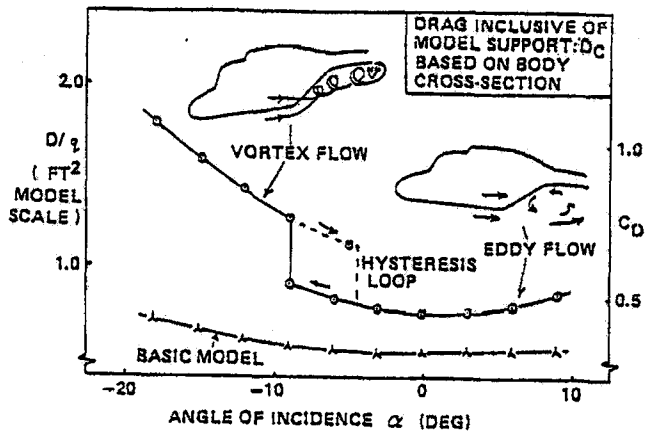

Fig. 2.5 Eddy flow/vortex flow transition effect on fuselage drag.

2.1.2. Influence of Engine/Gearbox Cowl Shape on Drag

The main purpose of the cowls is to contain engine and gearbox system. Beside this, they also provide area for the engine intakes to be positioned and optimized.

The influence of the cowls on fuselage drag is mainly due to their interaction with rotor head. Super velocity levels in the rotor head area increase the drag on cowls (Fig. 2.6). To decrease this effect, super velocity levels should be minimized by suitable contouring the forward of head.

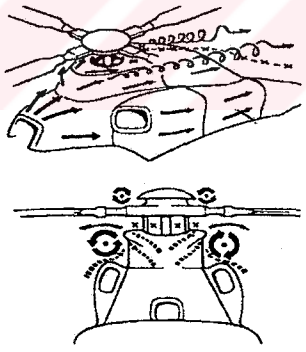

Fig. 2.6 Pylon and beanie aerodynamics on SA 365 N. [1]

2.1.3. Influence of Rotor Head on Drag

To decrease rotor head drag, frontal area of the rotor head should be minimized and low drag profiles should be employed which is shown in Fig. 2.7 [1]. The ultimate design is a complete head fairing.

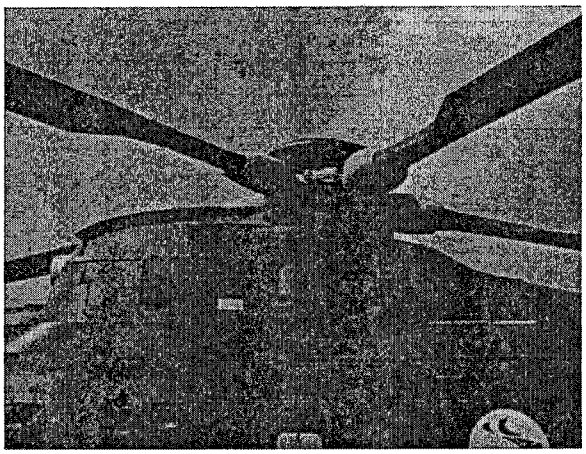

Fig. 2.7 Rotor head fairings and beanie. [1]

2.1.4. Influence of Engine Intakes/Exhaust on Drag

For low exhaust drag, spillage and external nacelle flow separation should be minimized. In addition, exhaust jet should be in downstream direction.

2.1.5. Influence of Empennage on Drag

Inverse cambered horizontal stabilizer minimizes the drag in the normal tail download condition in cruise flight. Cambered vertical fin decreases the drag of the rotor/fin combination in cruise flight.

2.2. Flow Separations Around a Helicopter Fuselage

Turbulent boundary layer separation is a major problem in flying vehicle aerodynamics, since they set upper limit for the vehicle performance. Existence of separation increases drag and decreases lift. Beside these, increase in vibration and noise can be observed.

In helicopter fuselage, usually juncture regions of the various aerodynamic components of the fuselage are responsible for the flow separation that entails the vortical structures. These vortical structures are formed by rolling up of the viscous flow sheet, previously confined in a thin layer attached to the wall, which suddenly springs into the outer non-dissipative flow. Usually horseshoe vortices form in these regions of the fuselage. Fillipone and Michelsen [5] studied on flow patterns on cowl and rotor head area of the helicopter fuselage numerically and experimentally.

2.2.1. Concepts of Separated Flow

Delery [6] studied on the structures of 3 dimensional separated flows and developed concepts for separated flows on curved surfaces [6].

For a two-dimensional flow, it is generally admitted that separation occurs when the skin friction τ_p goes to zero at a point S, which is called the separation point. Downstream of S a region exists where τ_p is negative, the velocity distribution along a normal to the surface obstacle surface including a portion where the longitudinal component u is opposite the main flow direction. The flow frequently reattaches some distance downstream of S in a point R where the skin friction passes through zero to become positive again. As shown in Fig. 2.8, the flow is organized as a recirculation bubble –often-called vortex- where the streamlines form closed curves. A special streamline called discriminating streamline originates in the separation point S and terminates in the reattachment point R. This streamline isolates the fluid trapped in the bubble from the fluid flowing from upstream infinity to downstream infinity.

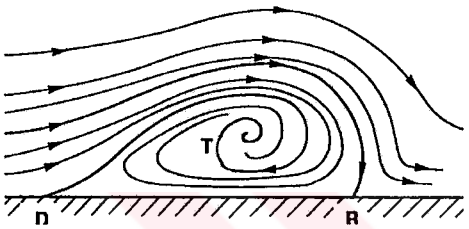

Fig. 2.8 2-D Flow Separation. [6]

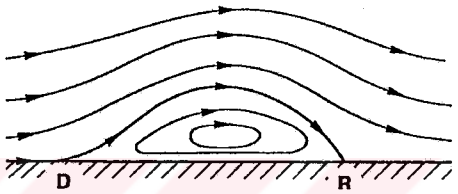

Fig. 2.9 3-D Flow Separation. [6]

In three-dimensional flows, the definition of separation as the zero crossing of the skin friction is inadequate and even ineffective. In effect, on a three dimensional obstacle there are generally no privileged directions along which the sign of the skin friction, which is now a vector, has a well defined physical meaning. Exceptions are some very special situations like a plane of symmetry or the case of an infinite swept wing. Furthermore, the three-dimensional flow has the capability of to develop transverse components allowing the fluid to escape laterally. Fig. 2.8 must be replaced by Fig. 2.9 where –in the plane considered- the streamline stagnating at the reattachment point R is distinct from the streamline emanating from the separation point S. the fluid flowing between these two lines escapes in vortex V.

Delery [6] explained the flow separation phenomena by critical point theory and gave flow topologies of trajectories around singular points (P_0) on the surface or in the flow. Trajectories are identified here by streamlines or skin friction lines. Mathematical concepts will not be given in the recent study, but the definitions of the topologies will be explained in this section.

If all trajectories, except one, have common tangent at P_0, then the singular point is a node (see Fig2.10). If all the trajectories have different slopes at P_0, the node is then said to be isotropic node (see Fig.2.11).

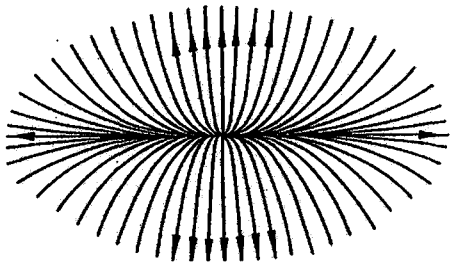

Fig. 2.10 Attachment Node. [6]

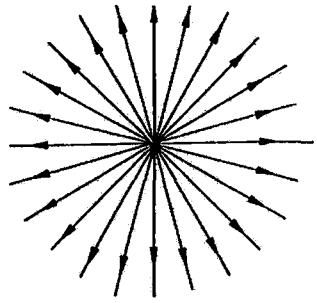

Fig. 2.11 Isotropic Node. [6]

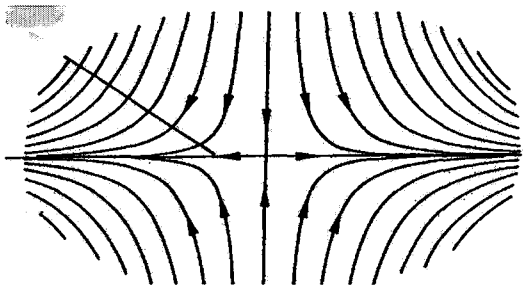

Fig. 2.12 Saddle Point. [6]

In the case that only two trajectories go through the singular point P_0, the other trajectories avoid P_0 and take on a hyperbolic shape; the singular point is called saddle point and shown in Fig. 2.12.

If all the trajectories end in the singular point and spiral around it they form focus (Fig. 2.13). If the singular point is not reached, then the trajectories are closed curves having the shape of an ellipse. This singular point is called center (Fig. 2.14)

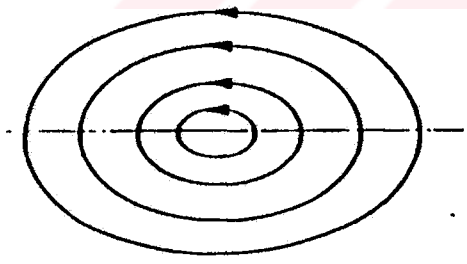

Fig. 2.13 Focus. [6]

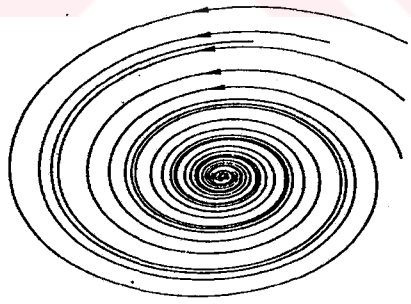

Fig. 2.14 Center. [6]

If there is infinite set of nodes and saddle points then the singular point is called saddle node (Fig.2.15)

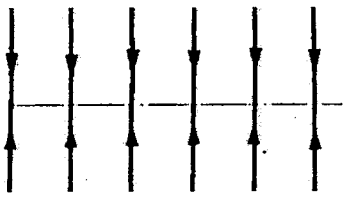

Fig. 2.15 Saddle Node. [6]

As shown in figures, trajectories in the vicinity of a focus or a node can be followed by moving either away from or towards the singular point. According to usual mathematical terminology, the critical point is called stable or unstable. In fluid mechanics, where trajectories are interpreted as streamlines or skin friction lies the singular point is called:

An attachment point if the fluid flows away from it.

A separation point if the fluid flows towards it.

Fig. 2.16 shows a schematic representation of the flow in the vicinity of a saddle point of separation. In this situation, the streamlines constituting what is called the separation surface (Σ) emanate from a node N –more precisely a half node- coincident with saddle point C. the streamlines of (Σ) flow away from N, the trace of (Σ) on the obstacle being the skin friction lines –constituting the separation line (S)- emanating from the saddle point. (See Fig. 2.16)

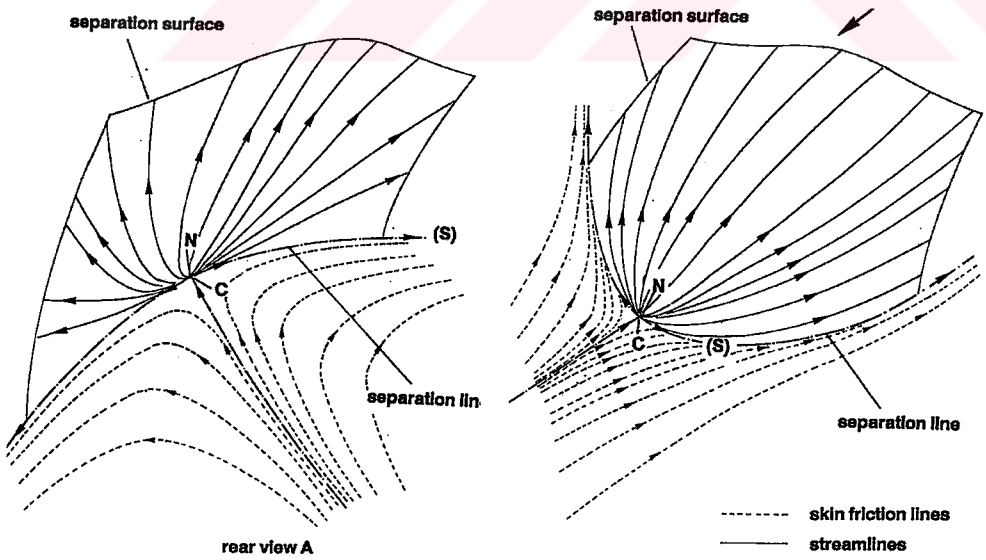

Fig. 2.16 Flow structure in the vicinity of a saddle point of separation. [6]

The situation at a saddle point of attachment is shown in Fig. 2.17. Now, what is called the attachment surface (Σ) is constituted by the outer flow streamlines flowing

in the direction of the node N coincident with C. In an attachment process, the attachment surface (Σ) passes through the skin friction lines- defining an attachment line (A)- going into the saddle point C.

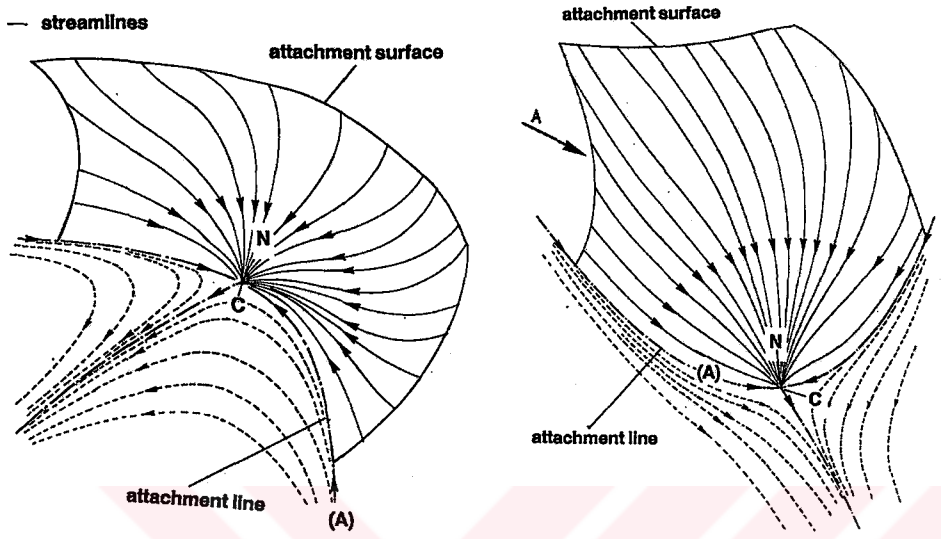

Fig. 2.17 Flow structure in the vicinity of a saddle point of attachment. [6]

In the case of separation, the separation surface (Σ) can be assimilated to what is called a separation or vortex sheet, although the concept of sheet –defined as a surface of tangential discontinuity for the velocity field- pertains to a perfect fluid model of the separated flow. In reality, for a viscous flow, the velocity and vorticity fields are continuous so that it is frequently difficult to define such sheet from inspections of experimental results.

Due its origin, the separation surface is located in a region of the filed where the vorticity tends to concentrate and the vortical structures can be interpreted as rolling up of the separation surface. Most often, a separation line (S) ends at a focus around which it spirals. This focus is the trace on the obstacle of the vortex resulting from the rolling up of the separation surface sustained by (S). Such a situation, with two foci, F_1 and F_2 , on either side of throat C, is depicted in Fig. 2.18. It corresponds to what tornado-like vortex. The focus sustaining the vortex can be in a plane of symmetry as seen in Fig. 2.19.

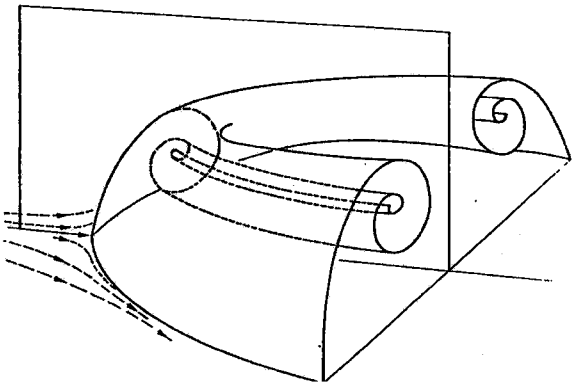

Fig. 2.18 Tornado-like vortex. [6]

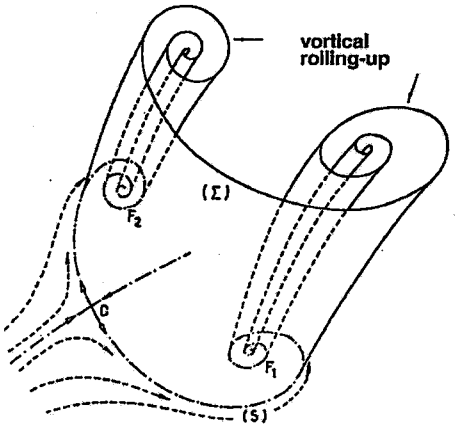

Fig. 2.19 Horseshoe vortex.[6]

3. EXPERIMENTAL SETUP AND TECHNIQUES

3.1. Introduction

In the present study, aerodynamics of an isolated helicopter fuselage was investigated by means of qualitative and quantitative methods. Qualitative flow properties around the fuselage were investigated by oil film visualization and smoke flow visualization with laser sheet methods. By qualitative visualization methods, flow behaviors at critical points of the fuselage were visualized to constitute basis for the quantitative measurements.

CTA measurements were conducted at the regions of the helicopter fuselage determined by the qualitative visualization experiments. By this experiment, quantitative values of velocity of the flow were obtained at the regions determined by visualization experiments.

Force and moment measurements were also conducted to obtain characteristic aerodynamic coefficients of isolated helicopter fuselage.

Flow similarity in helicopter fuselage experiments, depends on mainly on Reynolds Number, since viscous flows and separated flows exist on helicopter fuselages. Mach number similarity is not required, since the forward airspeed of present helicopters is well below the speed of sound and the flow is practically incompressible.

However, few data exist that would allow a direct comparison of a full-scale real fuselage with a scale model version. Reference [4] provides the example of a Bell 222 fuselage tested in Ames 40x80 ft wind tunnel and compares the results with those obtained on fifth scale models in the Vought 7x10 ft wind tunnel.

It was concluded that the most part of the differences observed between the measurements could be attributed to differences in the model support structures, whereas the Reynolds Number effects or geometrically modeling errors were much less significant. An example of results obtained is presented in Fig. 3.1 [4]. The comparison appears quite satisfactory, except high negative incidences. In conclusion, Reynolds number does not affect aerodynamic coefficients significantly except at high incidence angle regions.

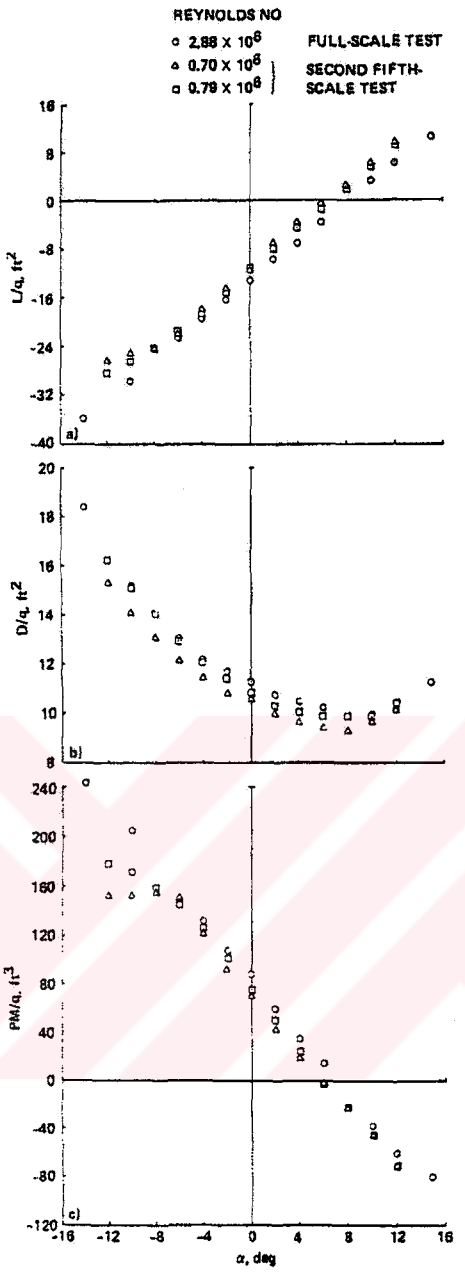

Fig. 3.1 Effect of Reynolds Number (based on horizontal stabilizer chord) on correlation for complete helicopter Bell tests. [4]

3.2. Wind Tunnels

In the recent study, Oil film visualization and balance measurements were conducted at Gümüşsuyu wind tunnel. Smoke flow visualization with laser sheet experiments and CTA measurements were conducted at Eiffel type wind tunnel.

3.2.1. Gümüşsuyu Wind Tunnel

Gümüşsuyu wind tunnel is a closed circuit low speed wind tunnel with a cross-sectional area of the test section of 80x110 cm. The tunnel contraction ratio is 9:1 and the streamwise turbulence intensity is less than 0.5% for the free stream velocity of 20 m/s in the test section. Schematic view of the tunnel is illustrated in Fig. 3.2.

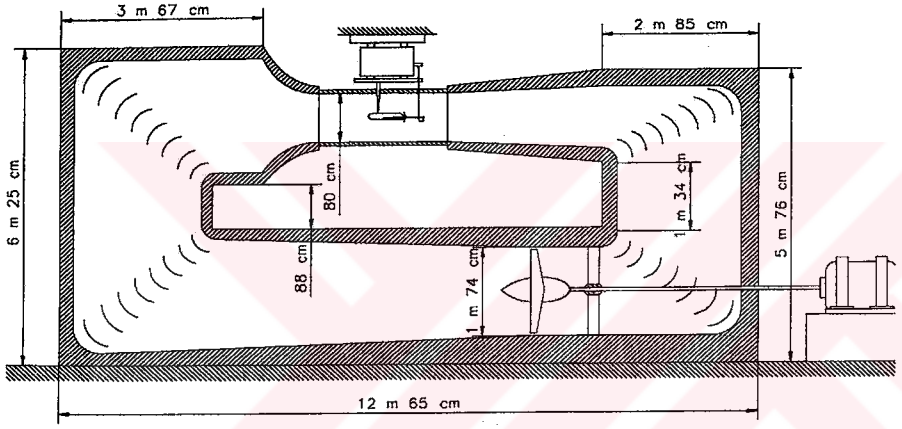

Fig. 3.2 Schematic view of Gümüşsuyu Wind Tunnel.

3.2.2. Eiffel Wind Tunnel

Eiffel Wind Tunnel is an open test sectioned, open circuit wind tunnel. Test section has a cross-sectional area of 80x80 cm. The streamwise turbulence intensity of the tunnel is 0.6% for the free stream velocity of 20 m/s.

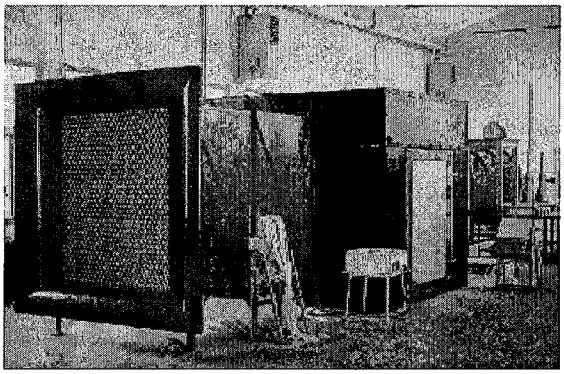

Fig. 3.3 Eiffel Type Wind Tunnel.

3.3. Models

Gill [7] gives detailed information about helicopter fuselage configurations according to nose and tail boom shape. He categorized nose shapes as symmetrical (N_S), droop (N_D) and cutback (N_H), tail boom shapes as high (T_F, T_E), full high straight (T_H) and full low cranked (T_L, T_C). Illustrations are represented in APP.A. According to these configuration definitions, models used in this study is defined as N_HT_F and N_DT_E.

Flow visualization experiments and CTA measurements were conducted with N_HT_F configuration model. Balance measurements were conducted with N_HT_F and N_DT_E configuration models.

3.3.1. N_HT_F Configuration Model

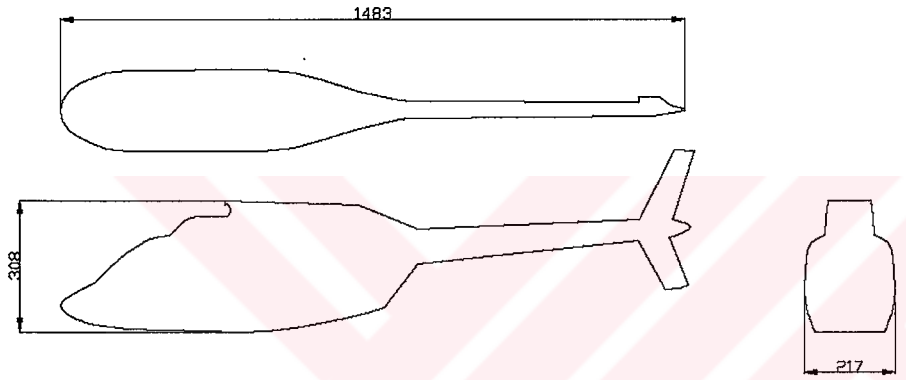

Fig. 3.4 N_HT_F Configuration Model.

Reference length l=1.483 m

Reference Horizontal projected area S_P= 0.148 m^2

Reference side projected area S_S=0.247 m^2

3.3.2. N_DT_E Configuration Model

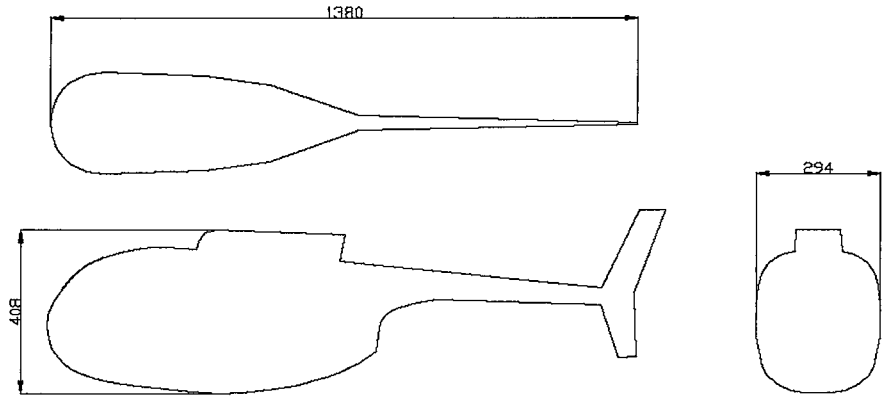

Fig. 3.5 N_DT_E Configuration Model.

Reference length l=1.380 m

Reference Horizontal projected area S_P= 0.153 m^2

Reference side projected area S_S=0.318 m^2

3.4. Flow Visualization Techniques

3.4.1. Smoke Flow Visualization

3.4.1.1 Seeding

The visualization of the flow in wind tunnels by means of smoke is a standard experimental tool for the work. The advancement of this technique is strongly related to development of the wind tunnels.

The term "smoke" is used here in a wide sense, not only restricted to combustion products and the discussion will include steam, vapor, mist and aerosols. From the usual requirement that one wants a tracer material to fulfill the below requirements:

- Being neutrally buoyant
- Being non-toxic
- Having low mixing rates with the main fluid.

Although the smoke fulfills none of these, it is the most convenient, because no better solution has been found yet.

The basic types of producing smoke are: burning or smoldering tobacco, wood or straw, vaporizing mineral oils; producing mist as the result of reaction of various chemical substances; and condensing steam to form a visible fog. Except the latter, all these substances are toxic to some degree. The density of these tracer materials is much larger than the density of the air., but since the particle size of the tracers is very small, mostly below 1 μm, sedimentation effects are minimized. Diffusion of the various types of smoke into the ambient air is much higher than diffusion of into water, so that streak lines can be identified over a reasonable distance only in laminar flow. An example is illustrated in Fig. 3.6 from [8].

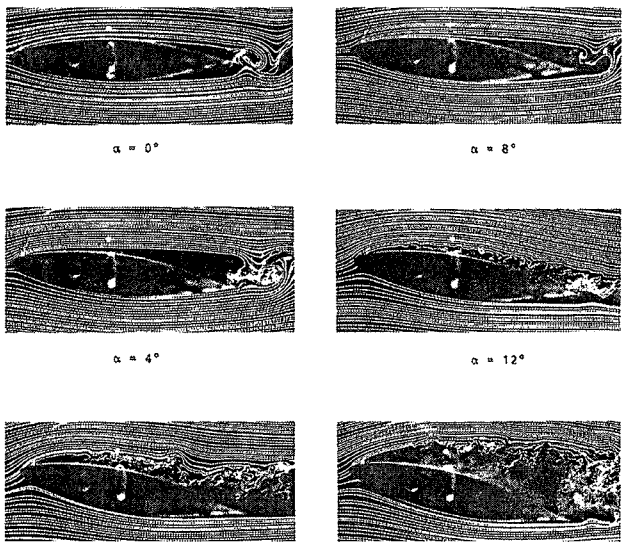

Fig. 3.6 Smoke-line visualization of the flow over an airfoil. [8]

A number of possible smokes and ways of their generation (Often called smoke-generators). Cigarette smoke has the finest tracer particles among all smokes. Kerosene mist probably is the most frequently used "smoke" for wind tunnel studies. The generation TiO_2 mist from $TiCl_4$ droplets deposited on the surface of a test model is not a direct injection method, bur rather a method of chemical controlled production of the trace material. The smoke-wire, an electrically controlled device, allows for the generation of very fine smoke lines. Direct injection of the smoke is performed by means of a smoke pipe or a system of such pipes.

The application of smoke to a recirculating wind tunnel creates the problem that, after a certain time of operation, the tunnel is completely filled with smoke. For this reason, and also because any smoke or aerosol is toxic to some extent, there is an interest in using steam or water fog as the trace material. Steam in combination with a cooling agent can be introduced in the airflow where visible fog is produced. After heat exchange with the surrounding air, the fog disappears, leaving the main air stream clean in the recirculating system. An air-drying device might be needed. Liquid nitrogen may serve as the cooling agent, so that the steam and the liquid nitrogen are expelled together into the air stream through a mixing nozzle. From preliminary experiments performed in relatively small wind tunnels, it has been reported that the visibility of such fog compares with that of TiO_2 mist or cigarette smoke; but the fog particles are larger than the particles of the two former materials.

For the reasons discussed in latter paragraph, many smoke flow experiments are performed in wind tunnels exhausting directly into the atmosphere. Injection of the smoke ahead of the contraction and a large contraction ratio serve to stabilize the smoke lines. In principle, there is no upper limit in air speed for the application of

smoke and smoke lines have been generated even in supersonic flows. Illumination in the smoke experiments is mostly conventional. Front light illumination under a certain angle with respect to the viewing direction with conventional resources such as mercury lamps, halogen lams, spot lights. More recently, illumination in form of a plane, thin light sheet is applied in order to visualize flow structures in a certain cross section of the flow field.

Beyond the use in wind tunnels, smoke flow visualization has been applies in any kind of air flows, even for large scale outdoor experiments or studies. Its special role for detecting separated flow regimes, vortices and coherent structures in shear layers.

3.4.1.2 Illumination by Light Sheet Methods

In this chapter, methods are discussed for which the illumination is provided in form of a plane, thin sheet, so that only the tracer material within thin sheet or slice is illuminated.

A light sheet can be produced with a conventional lamp. A much better way is to expand the beam from a powerful laser by means of a cylindrical lens in one plane. The thickness of such a sheet can be made much smaller than 1 mm. Observation of the flow pattern in the illuminated plane is normal to this sheet or under a certain angle. An example of experimental setup is given in Fig 3.7 from [8]. Illumination by a light sheet can be applied to both dye and smoke visualization and it is most appropriate to recognize vortical structures in these flows as shown in Fig 3.8 from [8].

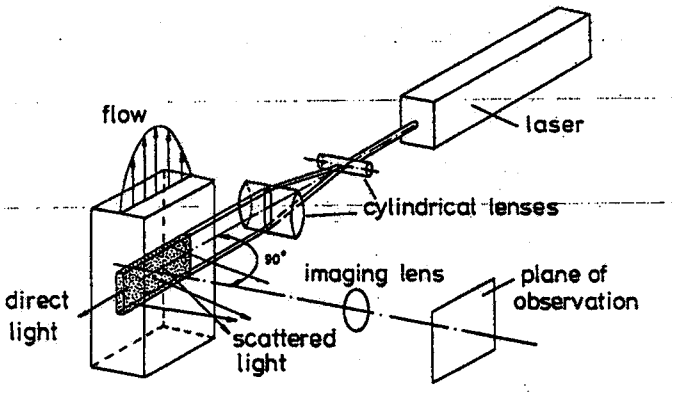

Fig. 3.7 Generation of a light sheet in a flow by expanding a laser beam. [8]

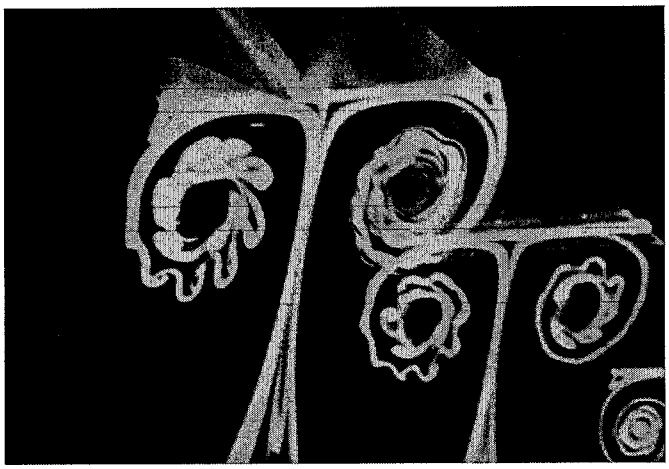

Fig. 3.8 Smoke visualization of leading edge vortices on a delta wing, illuminated by laser sheet. [8]

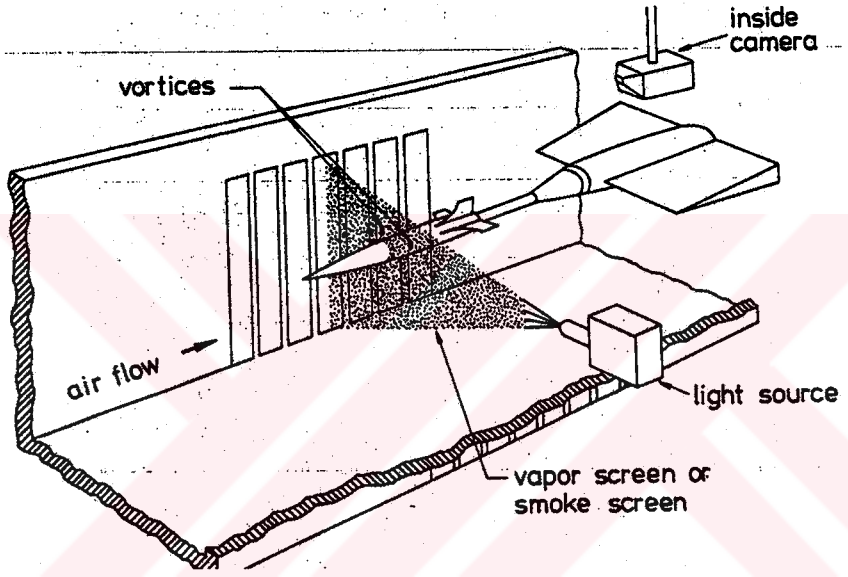

Fig. 3.9 Illumination by light sheet in a vapor tunnel or smoke tunnel. [8]

Flow facilities have been designed particularly for the application of a light sheet normal to the flow direction. These special wind tunnels are, to a certain degree, filled with either smoke or vapor and the technique is called smoke screen or vapor screen, respectively. They allow visualization of trailing vortices which separate from test models. A schematic view of the test section, light source, vapor or smoke screen and recording camera is shown in Fig. 3.9 from [8].

3.4.1.3 Purpose of The Experiments

The main purpose of the smoke flow visualization experiments is to determine the flow pattern topologies on the longitudinal cross-section of a helicopter fuselage fore body in different incidence angles. The secondary purpose is to evaluate them combining with the oil film visualization experiments' results to obtain separation

bubbles, attachment lines and vortices formed around the isolated fuselage of the helicopter model.

3.4.1.4 Experimental Setup

Open test sectioned Eiffel type wind tunnel was used for smoke flow visualization experiments (see section 3.2 for tunnel properties.). N_HT_F Configuration Model was used (see section 3.3.).

Smoke was generated by heating a glycol solution by a portable smoke generator. (see Fig. 3.10). 20 smoke filaments were introduced into the flow to improve flow-feature visibility. Smoke was divided into 20 filaments by a cylindrical pipe with 20 holes of diameter 2mm at its downstream sidewall, located at the test section inlet centerline horizontally.

A 5 W argon-ion laser was used to illuminate the section. Laser beam generated by laser generator went through a cylindrical lens to generate laser sheet of spreading angle of 40^0. A mirror was used to reflect the laser sheet for illuminating the upper part of the fore body of the fuselage. A high-resolution digital camera is used for capturing images of the experiment.

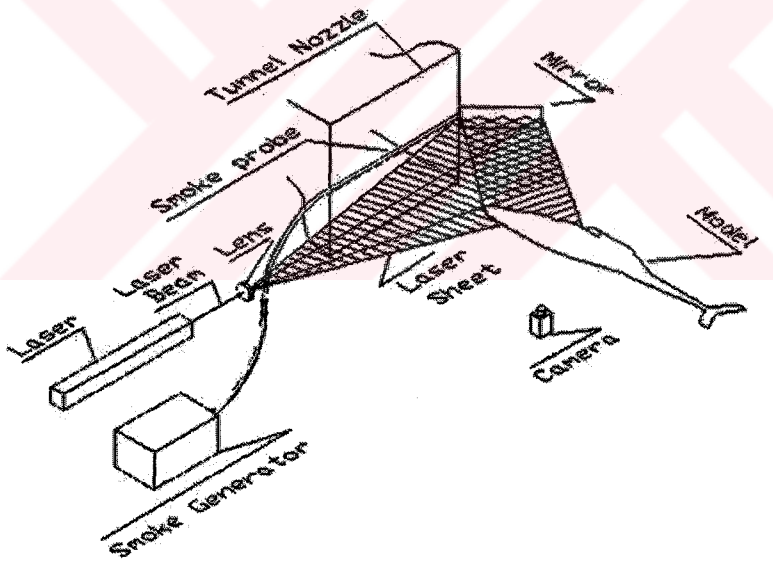

Fig. 3.10 Experimental setup for smoke flow visualization experiments of Bell Model.

3.4.1.5 Test Setup and Procedure

The model was aligned with the tunnel test section centerline. The tunnel airspeed has been chosen 5 m/s to obtain the model Reynolds number of $Re_l = 5.23125x10^5$. Reynolds number selection has been done according to the historical background and seeding capacity of our smoke generator. Dynamic pressure corresponding to this speed is 1.55 mmH_2O.

Experiments were done for incidence angles of 0^0 and 10^0. Images were taken at nose, nose cabin junction, cabin cowl junction and cowl regions of the forebody.

3.4.2. Oil Film Visualization

Since several decades of wind tunnel practice oil film visualization has become a standard wind tunnel technique. The surface of interest is coated with a thin layer of oil in which a finely powdered pigment is solved. When the wind tunnel is turned on, the oil is carried away with the air stream, and the dry pigment remains on the surface where it forms a streaky pattern indicating the direction of the flow close to the surface. Particular phenomena in the remaining pattern are attributed to flow separation from the surface or flow reattachment. A test model to which mixture of oil and pigment was applied can be taken out of the test section, after the tunnel has been stopped, and the pattern on the model surface can be inspected outside the wind tunnel.

Many instructions have been given in the literature on how to prepare an oil/pigment mixture appropriate for a specific test condition, e.g. [9] to [11]. A large amount of practical experience is collected and described in unpublished laboratory reports or manuals. The object is to prepare a mixture of such a consistency that it will run easily under the given test conditions and leave behind the desired streaks of the pigment. Ideally, the mixture should not begin to run until the selected wind speed is reached, and after an appropriate time of running, the pattern should be sufficiently dry to be unaffected by the unsteady airflow when the tunnel is stopped.

From the latter it follows, that the lower the air velocity, the lower should be the viscosity of the oil. Liquids, that have been used as solvents or carriers for the pigment, are, in ascending order of viscosity: alcohol, kerosene, and light diesel oil, light transformer oil. Viscosity and surface tension of these liquids can be adjusted by additives. Two special situations for modern wind tunnel testing should be mentioned: the low free stream pressures associated high speed wind tunnels are unfavorable for using standard oils, because these oils are characterized by high vapor pressures; then, vacuum pump oil is the right choice.

The pigment in the mixture should provide a clear pattern against the model surface as the background. A white powder like titanium dioxide (TiO_2) or china clay can be used on a dark model. Lampblack, a fine powder that mixes well with oil is most suitable on a light model surface. The dispersion of the pigment in oil may be improved by adding a few drops of oleic acid. Fluorescent pigments, when illuminated with ultraviolet light, can provide a very brilliant surface pattern; only

the surface pattern to be visualized is seen, whereas model and background remain invisible. This is of particular interest if the model geometry is complex.

The pigment pattern remaining on the model surface can be photographed for the purpose of recording it. If the model surface is curved, a problem comes up in relating the plane record of the curved surface pattern to surface coordinate system. As a solution of this problem, the model can be covered by a white, plasticized, self-adhering contact paper and oil-pigment (lampblack) can be applied to this cover. After the visible pattern is formed, the paper is separated from the wall and laid flat for being photographed. For the same purpose, i.e. for eliminating the camera parallax when photographing the surface pattern, transparent adhesive tapes can be applied to the model after the wind tunnel experiment. The very thin coating of pigment remaining on the surface is lifted off and preserved for taking a record.

The interpretation of the observed pattern is strongly related to the question on how pattern is formed. Several explanations have been given; but the problem has never investigated systematically. It has been said that the fine particles of the pigment coagulate, and that the striations are caused by the wake behind such coagulations in the flowing oil film. Hornung [12] observed that the flowing oil film becomes unstable, breaks up to form droplets, which due to their large resistance, shoot at high speed across the oil film, thus producing the striations. Murai et al. [13] verified longitudinal instabilities in the thin oil film, which could be responsible for the observed pattern.

Information on the accuracy of the oil film technique can be obtained if one analyzes the flow pattern in the oil film. The only available analysis has been developed by Squire [14]. He investigates the problem of how the airflow close to the wall is disturbed due to presence of the oil film. The boundary conditions for the airflow now have to be fulfilled at the oil/air interface where the velocity of the two fluids is the same and not zero. The velocity u at the interface is

$$u(y=h)=\frac{\mu_{air}}{\mu_{oil}}\left\{-\frac{h^2}{2}\left(\frac{1}{\mu_{air}}\frac{dp}{dx}+\left(h\frac{\partial u_{air}}{\partial y}\right)_{y=h}\right)\right\} \qquad (3.1)$$

where x is the streamwise coordinate in the plane of the wall, y is the coordinate normal to the wall, h is the oil film thickness, μ is the viscosity and p pressure. Since the ratio μ_{air}/μ_{oil} is of the order of 10^{-2} to 10^{-4}, u(y=h) is normally very small quantity, i.e., the change in the conditions for the airflow can be neglected, with the exception of one situation, namely, when the pressure change in streamwise direction, dp/dx, becomes very large. This, however, is the case at the location of flow separation or attachment, particularly if the separation is enforced by a shock wave. Squire's

analysis gives no information on how big the error in the measurement will be, e.g. in terms of the difference between the indicated and the real location of separation. But, since many oil film experiments are used for visualizing the positions of flow separation and attachment.

3.4.2.1 Purpose of The Experiments

The main purpose of the oil film visualization experiments is to determine the surface flow pattern topologies on a helicopter fuselage fore body in different incidence angles and sideslip angles. The secondary purpose is to evaluate them combining with the smoke flow experiments' results to obtain separation lines, attachment lines and vortices formed on around the isolated fuselage of the helicopter model.

3.4.2.2 Experimental Setup

Closed circuit Gümüşsuyu wind tunnel is used for oil film visualization experiments (see section 3.2 for tunnel properties.). $N_H T_F$ Configuration Model is invetigated (see section 3.3.) Kerosene (for decreasing the viscosity), machine oil (for increasing the viscosity) and lampblack (visualization element) mixture is applied to the surface of the model to visualize the surface patterns. A conventional spotlight does illumination. Images are taken by a high-resolution video camera in video format and then captured by PC capture card.

3.4.2.3 Test Setup and Procedure

The model was aligned with the tunnel test section centerline. The tunnel airspeed has been chosen 20 m/s to obtain the model Reynolds number of $Re_l = 2.0925 \times 10^6$ Reynolds number selection has been done according to the historical background. Dynamic pressure corresponding to this speed is 25 mmH_2O.

Experiments were done for sideslip angle of 15^0 at incidence angle of 0^0 and for incidence angles of -5^0, $0^0$and 10^0 at 0^0 sideslip angle.. After applying the mixture to the model, tunnel was run until the permanant flow topologies formed on the surface of the model. Images were taken at critical points of the fuselage forebody after the tunnel had been shut down.

3.5. Hot Wire Anemometry

3.5.1. Principles

Consider a thin wire mounted to supports and exposed to a velocity U as illustrated in Fig 3.11. When a current is passed through wire, heat is generated. In equilibrium,

this must be balanced by heat loss (primarily convective) to the surroundings. If velocity changes, convective heat transfer coefficient will change; wire temperature will change and eventually reach a new equilibrium.

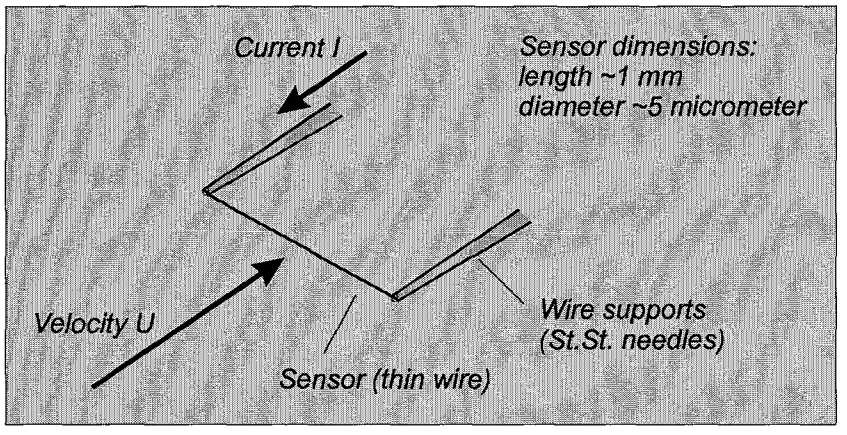

Fig. 3.11 Illustration of CTA Probe. [15]

Governing Equation:

$$\frac{dE}{dt} = W - H \tag{3.2}$$

E = thermal energy stored in wire

$$E = C_w T_s \tag{3.3}$$

C_w = heat capacity of wire

W = power generated by Joule heating

$$W = I^2 R_w \tag{3.4}$$

Recall $Rw = R_w(T_w)$ (3.5)

H = heat transferred to surroundings

Heat transferred to surroundings

$$H = \Sigma \begin{cases} \text{convection to fluid} \\ + \text{conduction to supports} \\ + \text{Radiation to surroundings} \end{cases} \tag{3.6}$$

Convection $Qc = N_u \cdot A \cdot (T_w - T_a)$ (3.7)

$N_u = h \cdot d/k_f = f(Re, Pr, M, Gr, \alpha)$ (3.8)

$Re = \rho U/\mu$ (3.9)

Conduction $f(T_w, l_w, k_w, T_{supports})$ (3.10)

Radiation $f(T_w^4 - T_f^4)$ (3.11)

For equilibrium conditions the heat storage is zero.

$$\frac{dE}{dt} = O \therefore W = H \qquad (3.12)$$

and the Joule heating W equals the convective heat transfer H.

Assumptions

-Radiation losses small

-Conduction to wire supports small

-T_w uniform over length of sensor

-Velocity impinges normally on wire, and is uniform over its entire length, and also small compared to sonic speed.

-Fluid temperature and density constant

Static heat transfer:

$W = H \Rightarrow I^2R_w = hA(T_w - T_a)$ $I^2R_w = N_u k_f/dA(T_w - T_a)$ (3.13)

h = film coefficient of heat transfer

A = heat transfer area

d = wire diameter

k_f = heat conductivity of fluid

N_u = dimensionless heat transfer coefficient

Forced convection regime, i.e. Re >Gr1/3 (0.02 in air) and Re<140

$$N_u = A_1 + B_1 \cdot Re^n = A_2 + B_2 \cdot U^n \qquad (3.14)$$

$$I^2R_w^2 = E^2 = (T_w - T_a)(A + B \cdot U^n) \qquad (3.15)$$

The voltage drop is used as a measure of velocity.

3.5.2. Velocity Sensitivity

Velocity sensitivity of CTA sensor is given in Fig. 3.12 and 3.13 for the values os coefficients A = 1.51, B = 0.811, n = 0.43

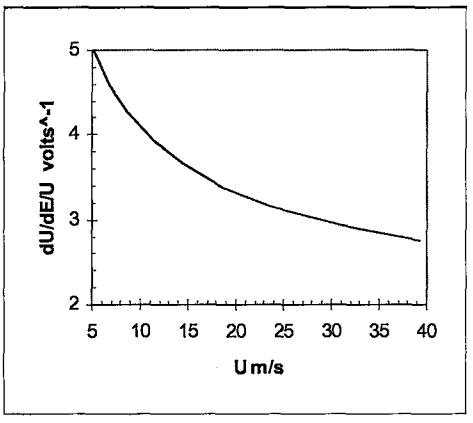

Fig. 3.12 Voltage change with respect to flow velocity. [15]

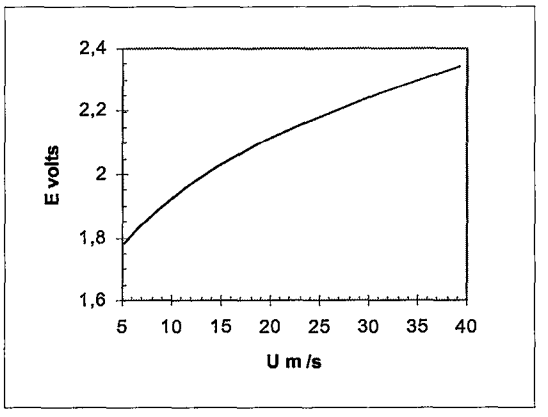

Fig. 3.13 Velocity sensitivity of CTA sensor. [15]

3.5.3. Directional Response

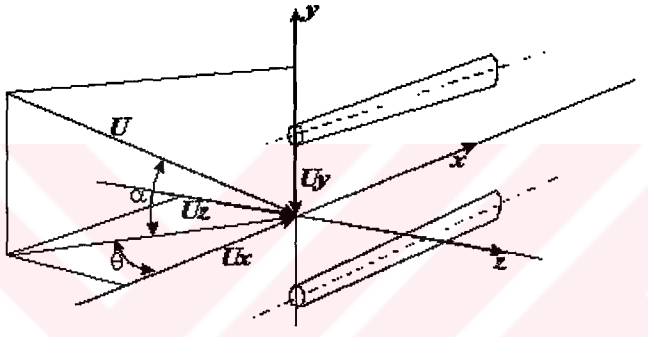

Fig. 3.14 Probe coordinate system. [15]

Velocity vector U is decomposed into normal U_x, tangential U_y and binormal U_z components as illustrated in Fig. 3.14.

Finite wire (l/d~200) response includes yaw and pitch sensitivity.

$U^2eff(a) = U^2(\cos^2 a + k^2 \sin^2 a)$ $\quad q = 0$ (3.16)

$U^2eff(q) = U^2(\cos^2 q + h^2 \sin^2 q)$ $\quad a = 0$ (3.17)

Where,

k, h = yaw and pitch factors

a, q = angle between wire normal/wire-prong plane, respectively, and velocity vector.

General response in 3D flows:

$$U^2_{eff} = U_x^2 + k^2 U_y^2 + h^2 U_z^2 \quad (3.18)$$

U_{eff} is the effective cooling velocity sensed by the wire and deducted from the calibration expression, while U is the velocity component normal to the wire.

Typical directional response for hot-wire probe is illustrated in Fig. 3.15.

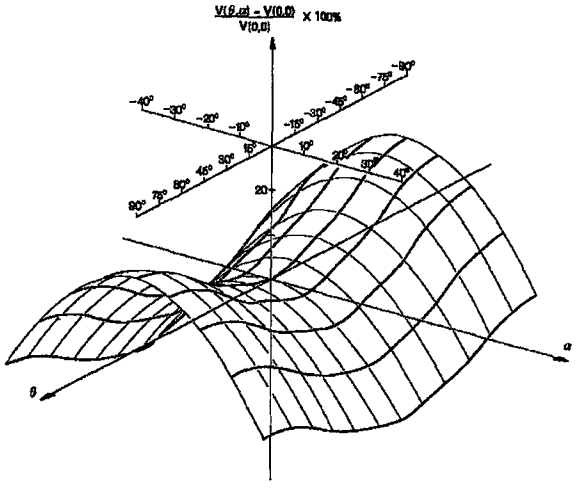

Fig. 3.15 Typical directional response for hot-wire probe. [15]

3.5.4. Basic Hot Wire Chain and Equations

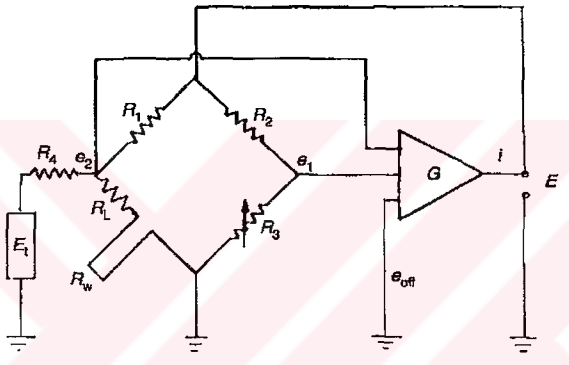

Fig. 3.16 Basic Hot Wire Chain. [15]

In Fig. 3.16 basic hot-wire chain is illustrated. In this chain, sensor resistance is kept constant by servo amplifier. Advantages of this chain are:

-Easy to use,

-High frequency response,

-Low noise.

Wire resistance can be written as:

$$R_w = R_o(1+\alpha_o(T_w-T_o)) \qquad (3.19)$$

R_w = wire hot resistance

R_o = wire resistance at T_o

α_o = temp. coeff. of resistance

T_w = wire temperature

T_o = reference temperature

OVERHEAT RATIO is defined as:

$$\alpha = (R_w - R_o)/R_o = \alpha_o(T_w - T_0) \quad (3.20)$$

Decade overheat resistor is set as: $RD = (1+\alpha)R_w$ (3.21)

The voltage across wire is:

$$E^2 = I^2R_w^2 = R_w(R_w - R_a)(A_1 + B_1U^n) \quad (3.22)$$

or as R_w is kept constant by the servoloop:

$$E^2 = A + BU^n \quad (3.23)$$

According to equations above CTA response is non- linear to velocity and increases with velocity. Beside, sensitivity decreases with increasing velocity.

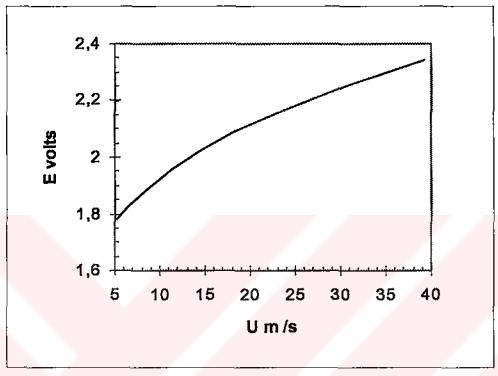

Fig. 3.17 CTA output as function of U. [15].

3.5.5. Velocity Calibration

Despite extensive work, no universal expression to describe heat transfer from hot wires and films exist. For all actual measurements, direct calibration of the anemometer is necessary.

Calibration in gases is done by low turbulent free jet. An illustration of equipment for calibrating CTA probe by low turbulent free jet is illustrated in Fig. 3.18.Velocity is determined from isentropic expansion.

$$P_o/P = (1+(\gamma-1)/2M^2)^{\gamma/(\gamma-1)} \quad (3.24)$$

$$a_0 = (\gamma PT_0)^{0.5} \quad (3.25)$$

$$a = a_o/(1+(\gamma-1)/2M^2)^{0.5} \quad (3.26)$$

$$U = M.a \quad (3.27)$$

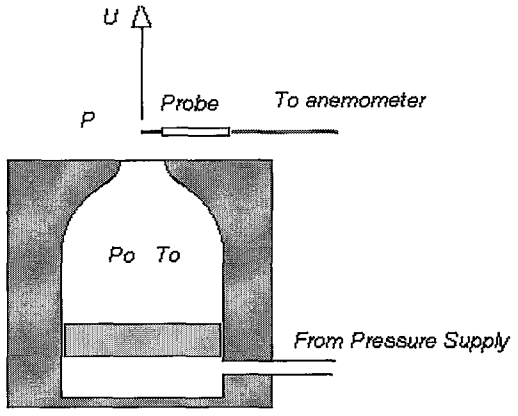

Fig. 3.18 Calibration Equipment. [15]

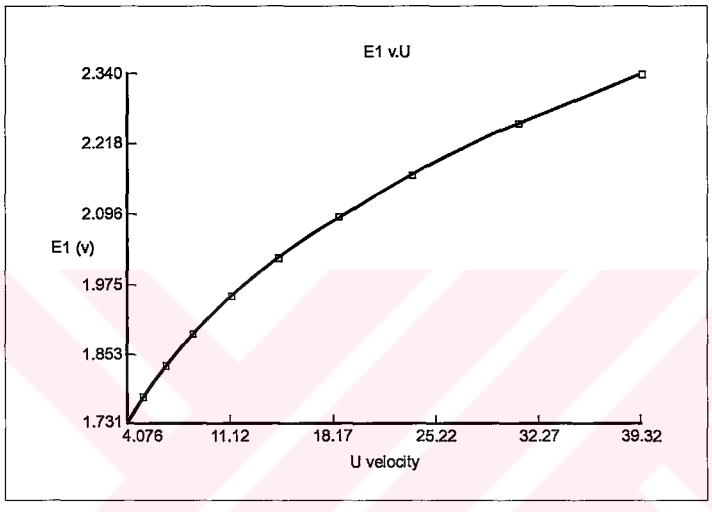

Fig. 3.19 Typical calibration curve. [15]

Curve fit of velocity U as function of output voltage E is,

$$U = C_0 + C_1E + C_2E^2 + C_3E^3 + C_4E^4 \qquad (3.28)$$

3.5.6. Dynamic Calibration/Tuning

3.5.6.1 Direct Method

In this method, a flow in which sinusoidal velocity variations of known amplitude superimposed on a constant mean velocity is needed. Microwave simulations of turbulence (<500 Hz), sound field simulation of turbulence (>500 Hz), vibrating the probe in a laminar flow (<1000Hz) are procedures for direct dynamic calibration. But all these methods are difficult and are restricted to low frequencies

3.5.6.2 Indirect Method "Square Wave Test"

In this method, the sensor is subjected to an electric sine wave, which simulates an instantaneous change in velocity, and the shape of the anemometer output is analyzed.

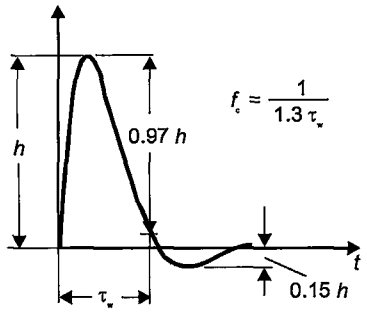

Fig. 3.20 Square wave test response of anemometer. [15]

3.5.7. Data Acquisition

Data acquisition, conversion and reduction require digital processing based on selection of proper A/D board, signal conditioning, proper sampling rate and number of samples, A/D boards convert analogue signals into digital information (numbers).

They have following main characteristics:

-Resolution of min. 12 bit (~1-2 mV depending on range)

-Sampling rate of Min. 100 kHz (allows 3D probes to be sampled with approx. 30 kHz per sensor)

-Simultaneous sampling. If not sampled simultaneously there will be phase lag between sensors of 2- and 3D probes

-External triggering allows sampling to be started by external event

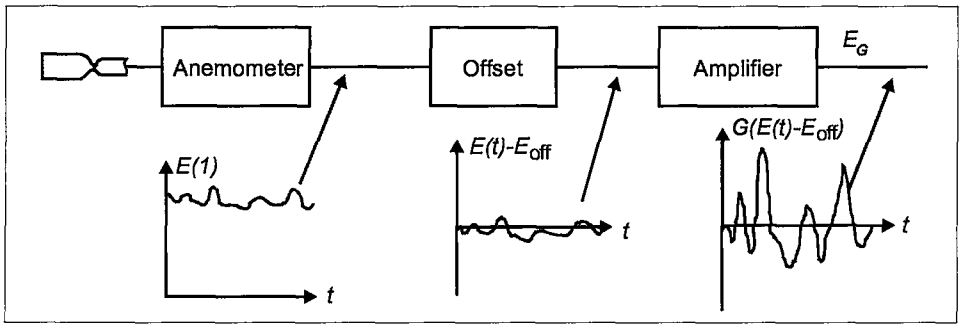

Fig. 3.21 Signal Conditioning of anemometer output. [15]

Signal conditioning of anemometer output increases the AC part of the anemometer output and improves resolution, allows filtering of anemometer. Schematic view of anemometer signal conditioning is illustrated in Fig. 3.21.

$$EG(t) = G(E(t) - Eoff) \quad (3.29)$$

Sample rate and number of samples should be chosen according to these criteria,

-Time domain statistics (spectra) require sampling 2 times the highest frequency in the flow

-Amplitude domain statistics (moments) require uncorrelated samples. Sampling interval min. 2 times integral time scale.

-Number of samples shall be sufficient to provide stable statistics (often several thousand samples are required)

3.5.8. Purpose of The Experiments

The purpose of CTA measurements is to determine velocity magnitudes and separation regions near helicopter fuselage and to compare results with the flow visualization results.

3.5.9. Experimental Setup

Open test sectioned Eiffel type wind tunnel was used for CTA measurement experiments (see section 3.2 for tunnel properties.). N_HT_F configuration model was used (see section 3.3.)

Dantec dynamics traverse system working cooperative with data acquisition software was employed for probe positioning. Single sensor 55P12 probe, which has a turbulence intensity of 25-30 % was used (Fig. 3.22). Probe has been mounted to 55H20 support (Fig. 3.23) 55H137 guide tube by 55H136 chuck (Fig .3.24). National Instruments AT/PCI-MIO-16E-4 A/D board has been used to convert analog data to digital values with gain value of 0- 10 V. Low Pass filter of signal conditioner was set to 0.3 KHz with sampling frequency of 2.1 KHz and 2048 measurements at each point .

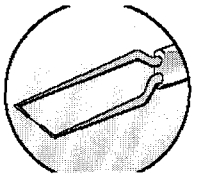

Gold-plated wire probe: 55P02
Fiber-film probes:
Thin quartz-coating: 55R02
Heavy quartz-coating: 55R12

Fig. 3.22 55P02 probe. [15]

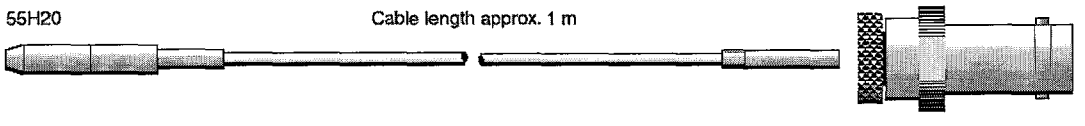

Fig. 3.23 55H20 Probe support. [15]

Fig. 3.24 55H137 guide tube and 55H136 chuck. [15]

3.5.10. Test Setup and Procedure

The model was aligned with the tunnel test section centerline. The tunnel airspeed has been chosen 15 m/s to obtain the model Reynolds number of $Re_l = 15.69375x10^5$. Dynamic pressure corresponding to this speed is 14.025 mmH_2O.

Experiments were done for incidence angles of -10^0, 0 and 10^0. Measurements were taken at the forebody region between nose and cowl at the central cross-section.

3.6. Force and Moment Measurements

3.6.1. Introduction

One way to determine the forces acting on a model under experimental conditions is to measure the pressure distribution on the surface of the model and integrate. But more convenient way to determine the forces is to measure them directly by a balance mechanism. By determination of the projectile of forces on the balance coordinate system, these quantities can be transformed to other coordinate systems. (Fig. 3.25)

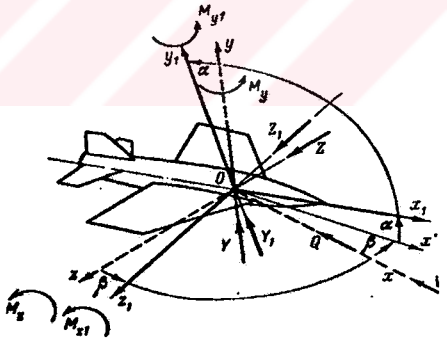

Fig. 3.25 Coordinate system transformation. [16]

Balance system has various types according to their placement, number of components they measured and the measuring devices located on.

Number of components measured can vary from 1 to 6 according to problem. If the case is two dimensional, then 3 components (lift, drag, pitching moment.) will be enough. So 3-component balance system is adequate to achieve the measurements. However, in three-dimensional problems, balance system has to achieve 6-component measurement (lift, drag, side force, pitching moment, yawing moment and rolling moment.).

Wind tunnel balance systems can be determined in two groups according to their placements. Systems that are placed out of the test section of the tunnel and model are included in the first type and systems that are placed inside the model or on the supporting rods, are included in the second type. First type of balance systems is called mechanical balances, since they include complex mechanisms for measurements. If the acting forces are transformed to electrical signals then these balances are called electro-mechanical balances.

In the external balances, model is generally connected to balance system by supporting rods. Disadvantage of this configuration is existence of supporting rods in the flow. This means that these rods affect flow and some aerodynamic forces are acting on these rods. If necessary, investigations on these affects and corrections have to be done.

In external balance systems, forces and moments are determined according to balance coordinate system. If sideslip angle is present, then forces and moments must be transformed from balance coordinate system to flow coordinate system.

Internal type balance systems, which are placed inside model, don't require support rods. Beside, it is impossible to locate the internal balance mechanisms into the model in high-speed small size test section wind tunnels, since model is also small sized. In this condition, internal balances with strain gages are employed.

The basic principle of strain gages is the measurement of the deformation caused by the forces and moments acting on the supporting rod. Deformations are transformed to electrical signals and these signals are transformed to forces and moments according to calibration of the strain gages. The most important advantage of measurement by strain gages is that they respond rapidly to changes in acting forces and moments. This respond time enables measurement of high frequency vibrations.

3.6.2. Principles

Besides lift, drag, and pitching moment, the aircraft is subjected to rolling moment, yawing moment and side-force. This makes a total of six measurements in all; three forces, mutually perpendicular, and three moments about mutually perpendicular axes. The wind tunnel balance must separate out these forces and moments and accurately present the small differences in large forces, all without appreciable model deflection.

In order to picture the situation clearly, an impractical wire balance based on readings made with spring scales is shown in Fig. 3.26. The model, supposedly too heavy to be raised by the lift, is held by six wires and six forces are read by the scales A, B, C, D, E and F.

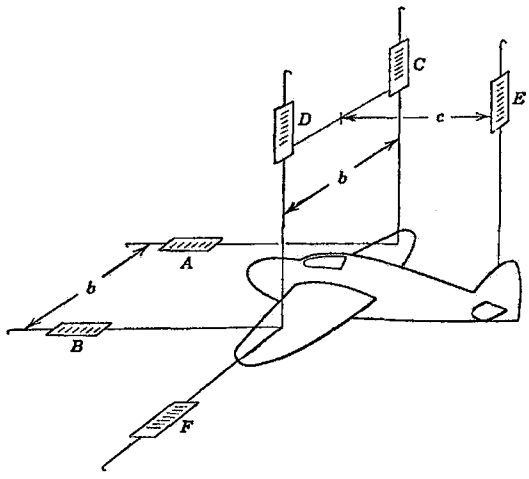

Fig. 3.26 Diagrammatic wind tunnel balance. [16]

1. Since the horizontal wires A, B and F cannot transmit bending, the vertical force (the lift). $-L = C + D + E$ (3.30)

2. The Drag $D = A + B$ (3.31)

3. The Side Force $S = F$ (3.32)

4. If there is no rolling moment, scales C and D will have equal readings. A rolling moment will appear as $R.M. = (C-D) \times b/2$ (3.33)

5. Similarly yawing moment $Y.M. = (A-B) \times b/2$ (3.34)

6. The pitching moment $M = E \times c$ (3.35)

Exact perpendicularity between the components must be maintained. For instance, if the wire to scale F is not exactly perpendicular to wires A and B, a component of drag will appear as side force. A similar situation exists in regard to lift and drag and lift and side force.

Four types of wind tunnel balance according to their mechanical structure are in general use, each processing certain advantages over the others. These balances are named from their main load-carrying members –wire, platform, yoke and pyramidal

3.6.2.1 Pyramidal (Virtual Center) Balance

Pyramidal balance reads the moments about the model, and six components are inherently separated out and read directly by six measuring units. No components need to be added, subtracted or multiplied. Difficulties involved in reading the small

differences in large forces are eliminated and direct reading of the forces and moments simplifies the calculating equipment.

The manner in which the pyramidal balance separates out the moments is not simple. Consider a truss in which two legs are joined (Fig. 3.27). The force D, acting through the pin joint, produces only tension in OE and compression in OF. No force is registered in A. However the force G, not acting through O, produces bending in OE and OE would collapse unless the force A=aG/b were present. If G and b are known, the force A determines the point of action of G. In this manner, if G were a known drag force, its pitching moment about the resolving center = would be determined by the force A.

Through the above example illustrates the principle of the pyramidal balance, in actual practice a considerable revision is required. In order to prevent the legs of the pyramid from being in the air flow, they are cut off as in Fig. 3.28. The truncated legs are then carefully aligned so that their extensions pass through the common point O. The complete setup is illustrated in Fig. 3.28.

Lift = total weight on the lowest table (3.35)

Drag = D (3.36)

Side force = -C (3.37)

Rolling moment = R x f (3.37)

Pitching moment = -P x f (3.39)

Yawing moment = Y x a (3.40)

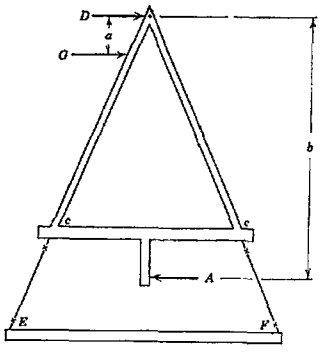

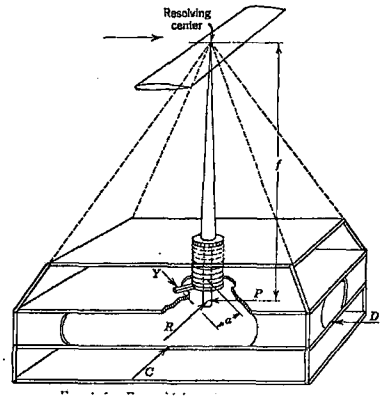

Fig. 3.27 Principle truss system. [16]

Fig. 3.28 Pyramidal (virtual center) balance. [16]

3.6.3. Strut Effects

Any strut or wire connecting the model to the balance will add three quantities to forces read. The first is the obvious drag of exposed strut or wire; the second is the

effect of the strut's presence on the free airflow about the model; and the third is the effect of the strut on the free airflow about the model. The last two items are usually lumped together under the term "interference" and their existence should make clear the impossibility of evaluating the total tare by the simple expedient of measuring the drag on struts with the model out.

3.6.4. Balance Calibration

Whatever the balance type and whatever the type of mounting employed, the rigging of the balance must be checked that the elements are mutually perpendicular and the forces remain properly separated. Ana arrangement that will accomplish this checking is shown in Fig.3.29. With this rig, various loads and moments can be applied separately, and the independence of the readings as well as accuracy can be determined.

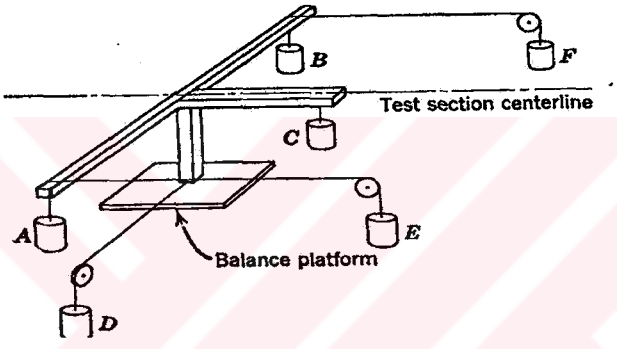

Fig. 3.29 Setup for balance calibration. [16]

The weights should be progressively added to one component, and all six components should be read. In this way the amount of, say, lift in the other components may be noted. Then a large load should be added, say drag, and the effect on the lift should be noted. With the added load still on, lift should be recalibrated; this will indicate changes in calibration due to extraneous loads. At various times, during the calibration, very small weights should be added to evaluate the changes of sensitivity due to load.

The above process should be repeated with all components and adjustments and corrections should be made until the accuracy and calibration are known.

3.6.5. Force and Moment Measurement Experiments

3.6.5.1 Experimental Setup

N_HT_F and N_DT_E configuration models are used. Detailed information of models is given in section 3.3. Force and moment measurements took place in Gümüşsuyu

Closed circuit wind tunnel (See section 3.2). The balance manufactured by TEM engineering ltd. has done the measurements. Matlab software created acquires data.

3.6.5.2 TEM Balance

The balance used in this research is an external electro-mechanical, virtual center balance with 6 degrees of freedom, manufactured by TEM engineering Lmtd. Drag, lift, side forces, yawing, pitching and rolling moments can be measured independently from each other. It has a wide range of loading intervals. For more information about balance systems, refer to [5].

Coordinate system of the balance rotates with yawing angle but doesn't rotate with pitching moment.

Assuming the lift acting on the model is upwards makes direction assumption for the forces and moments. According to this assumption, drag is positive towards downstream, side force is positive towards left, yawing moment is positive heading left, rolling moment is positive forcing right side of the model down, pitching moment is positive forcing head down. Beside direction of these loads, they must not exceed some limits. These limits are called standard load limits and are given Table 3.1.

Table 3.1 Standard Load limits of TEM balance. [17]

Component	S.I.	METRIC	IMPERIAL	ERROR (percent of full range)
Lift	0-220N	0-23kgf	0-50lbf	+/-0.1%
Drag	0-67N	0-7kgf	0-15lbf	+/-0.1%
Side Force	+/-135N	+/-13.5kgf	+/-30lbf	+/-0.25%
Pitch	+/-11Nm	+/-1.1kgf	+/-100lbf in	+/-0.1%
Roll	+-3.5Nm	+/-0.35kgf	+/-30lbf in	+/-0.25%
Yaw	+/-3.5Nm	+/-0.35kgf	+/-30lbf in	+/-0.25%

Components of TEM balance are model support rods, moving frames that measure forces acting on the model and to which support rods are connected, mechanisms that

separate the forces acting on the frames to components. Mechanism that change angle of incidence and yawing angle, transducers transforming forces to electrical signals for data acquisition. Scheme of TEM balance is given in Fig. 3.30.

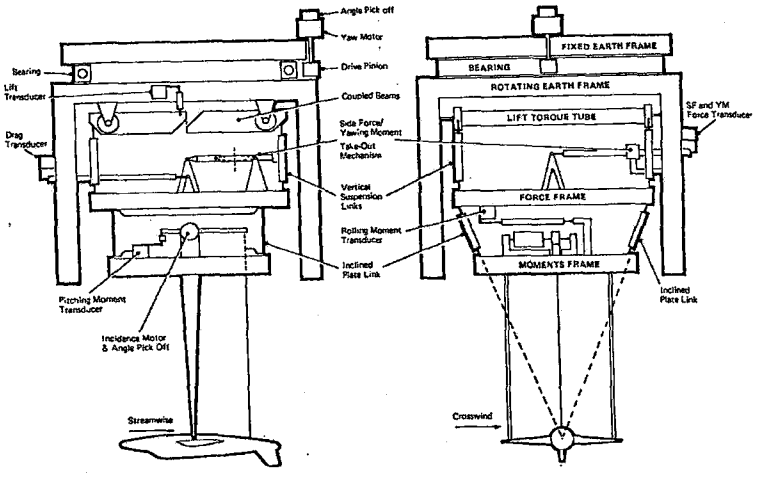

Fig. 3.30 Schematic view of TEM balance. [17]

A fixed earth frame, bolted to the wind tunnel structure, supports a bearing ring on which the rotating earth frame revolves about a vertical axis. Pivoted on the rotating earth frame are two torque tubes carrying a coupled beam lift system, which supports the forces frame via four vertical links. The moments frame is attached to the forces frame by a pair of inclined plates. Incorporated in the frame are the main strut platforms the incidence positioning equipment, the tail strut mounting and the pitching moment measuring system. Suitably positioned load transducers and links are coupled to various frames so that the six components of force and moment are independently measured about axes that yaw but do not pitch with the model.

Lift: Any vertical or lifting force experienced by the model is transferred via the inclined plate links to the forces frame. This force then acts on the coupled beams via the vertical suspension links. The lift torque tube provides resisting force against which the coupled beams move and the lift transducer provides an electrical output that is linearly proportional to the force exerted on the model.

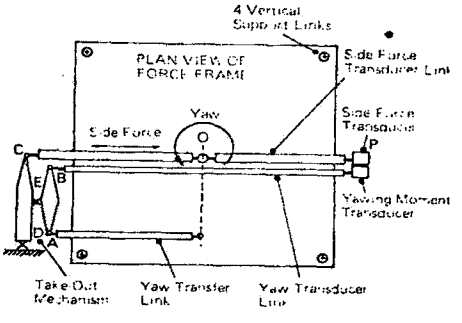

Fig. 3.31 Yaw and side force take out mechanism. [17]

Drag: Any drag or horizontal streamwise force on the model exerts a corresponding force on the moments frame and this is transferred to the forces frame by means of a shear force in the inclined plate links. The movement between the forces and the earth frame is horizontal by virtue of the four vertical supporting flexures. This movement is resisted by the horizontal drag link and transducer, from which an appropriate electrical signal is obtained.

Side Force and Yawing Moment: the side force and yawing moment are resisted by the links OP and AY respectively, as shown in the diagram. The reactions between the forces in these links that require the use of a take out linkage in order that separate measurements of these two components can be obtained from the two transducers mounted on the earth frame.

Takeout linkage consists of inner and outer levers, AEB and DEC respectively. The former pivots about the common center point E, whilst the latter pivots about D on the earth frame as illustrated in Fig. 3.31.

Pitching Moment: A pitching moment applied to the model is transferred, as a load in the tail strut, to the incidence mechanism mounted on the moments frame, and tends to rotate the former about a horizontal crosswind axis. Such movement is resisted by the transducer mounted on the moments frame and coupled to the incidence mechanism by a horizontal streamwise link. The tail strut remains vertical because it is a part of a parallel motion system that includes the model and the incidence arm.

Rolling Moment: A rolling moment applied to the model is transferred via the model struts on the moments frame, which tends to rotate about the virtual axis formed by the intersection of the planes of inclined plates. This movement is resisted, and the rolling moment is measured by the transducer mounted on the forces frame and coupled to the moments frame by a horizontal crosswind link.

Load Transducers and Flexures: Each of six transduces has a flexure presicion machined from a solid block of metal. This compromises a spring system ,carriers for the Linear Voltage Differential Transformer (LVDT) and its slug, a pick off point from a load link and an attachment for a damper paddle. A dashpot, separately mounted on the base plate of the transducer, provides damping when filled with suitable oil (Fig. 3.32).

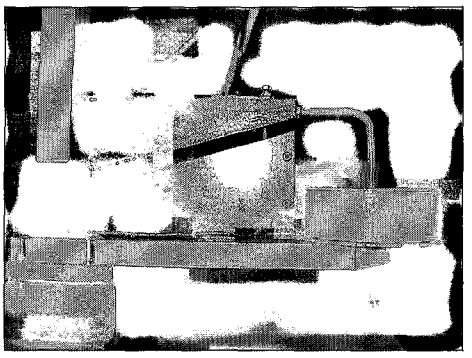

Fig. 3.32 Load transducer and flexure of TEM balance.

3.6.5.3 Data Acquisition Card

Data has been acquired by PCL-818H data acquisition card. Key features of the card is as fallows [18]:

1. A switch selectable analog input channel configuration of either 16 single ended or 8 differential inputs.
2. An industrial standard 12-bit successive approximation A/D converter is used to convert the analog inputs. The highest A/D sampling rate is 100 KHz in DMA mode.
3. Remote programmable analog input range setting with software control. Each channel has its own range setting and this setting is stored in an on-board RAM.
4. Software Selectable analog input ranges.

   Bipolar : ±0.625 V, ±1.25 V, ±2.5 V, ±5 V, ±10 V.

   Unipolar : 0 to +1.25 V, 0to +2.5 V, 0 to 5 V, 0 to 10 V.
5. The analog input-range control codes are stored in an on-board RAM. This feature enables the PCL-818H to change the range for each channel automatically when channel switching without CPU programming of the PC.
6. Three A/D trigger modes: Software trigger, programmable pacer trigger and external pulse trigger.
7. A/D conversion data can be transferred by program control, interrupt handler routine or DMA transfer.
8. An Intel 8254 Programmable Timer/Counter provides pacer (trigger pulses) at rates from 2.5 MHz to 0.00023 (71 minutes/pulse). The time base is switch selectable: 10 MHz or 1 MHz. One 16-bit counter channel is reserved for user configuration applications.

9. One 12 bit monolithic multiplying D/A output channel. An output range of 0 to 5 V (10 V) can be generated using the on board –5 V (-10 V) referenceV An external AC or DC reference can also be used to generate other D/A output ranges.
10. 16 digital input and 16 digital output channels, all of which are TTL/DTL compatible.

Selection of the range codes determines the sensitivity of the measurents. To select range codes for an experiment, maximum loads exerted on the model for each channel must be determined. Since the range codes determine the upper and lower limits of the voltage readings of the card, maximum loads exerted on the model should be in these ranges. Range codes divide the selected range to 4096 digit values (LSB Values). Sensitivity ratios and load sensitivities for range codes are given in tables 3.2 and 3.3

Table 3.2 Sensitivity ratios for range codes. [19]

Range Code	Sensitivity Ratio mV/LSB)
+/-5V	2,44
+/2,5V	1,22
+/-1V	0,49
+/0,5V	0,24
0,+10V	2,44
,+5V	1,22
0,+2V	0,49
0,+1V	0,24
+/-10V	4,89

Table 3.3 Load sensitivities for range codes. [19]

Range Code	Smallest Load Able to be Measured (gr)
+/-5V	24,4
+/2,5V	12,2
+/-1V	4,9
+/0,5V	2,4
0,+10V	24,4
,+5V	12,2
0,+2V	4,9
0,+1V	2,4
+/-10V	48,9

Example:

For +-10 V, 1 LSB=(10+10):4096=0.00488 V

Which means, 0.00488 V change in Volts corresponds to 1 LSB change.

For the recent study selected range codes are as follows:

Roll:	±2.5 V	Side Force:	±1.25 V
Pitch:	±2.5 V	Lift:	±1.25 V
Drag:	0-1.25 V	Yaw:	±2.5 V

3.6.5.4 Calibration of TEM Balance

Every measurement device needs to be calibrated before every acquisition. As a result of calibration, a matrix is obtained that transforms the voltage values read from the balance to force and moment quantities. This matrix is used as transformer during data acquisition.

Since this matrix is dependent on the environmental conditions and characteristics of the balance, recalibration of the balance is needed if these conditions change.

To calibrate TEM balance, known forces and moments are applied to the balance and these values are entered to computer and digit values are read by using Matlab software and are saved to a file. The output of these files is given in APP.B. Then the transducer calibration coefficients and interaction coefficients are calculated by these data.

Simple equation of calibration is given below.

$$R = a.[R_M + \sum b_i.I_i] \qquad (3.29)$$

a : Calibration coefficient of transducer

b : Interaction coefficient of other transducers

R : Interested Force or moment in engineering units

R_M : Raw data of interested force or moment

I : Raw data read from other transducers.

Method of applying forces and moments is given Fig. 3.33.

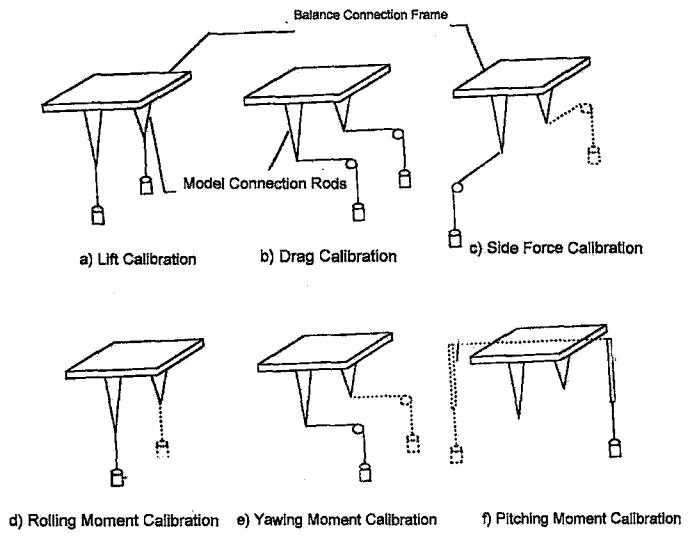

Fig. 3.33 Application of calibration loads.

As mentioned before, loads applied to balance should not exceed balance limits. These limits are called are called standard load limits and they have different values for each force and moment. Thus, voltage values corresponding to each load limit is different. So the voltage interval of each channel should be different for the sake of sensitivity. These voltage interval are called range codes. The smaller the range code, the more sensitivity obtained. However, maximum value of range code should not be smaller than the maximum value to be measured and minimum value should not be greater than the minimum value to be measured, since voltage values exceeding these limits will not be measured. So selection of range codes should be achieved according to maximum and minimum loads that the model will be go under during experiment.

Voltage values that are coming from each channel and produced by the balance, is transformed to digit values since the compter can define. These digit values are called LSB and vary fron –2048 to 2048 or 0 to 4096. This means that range code value is divided to 4096 intervals and each interval correspons to a porticular voltage value.

Selection of smaller range codes resulting in smaller LSB/Voltage ratio, enables more sensitive measurement of voltage changes.

Calibration curves of six tranducers are given in Fig.3.34.

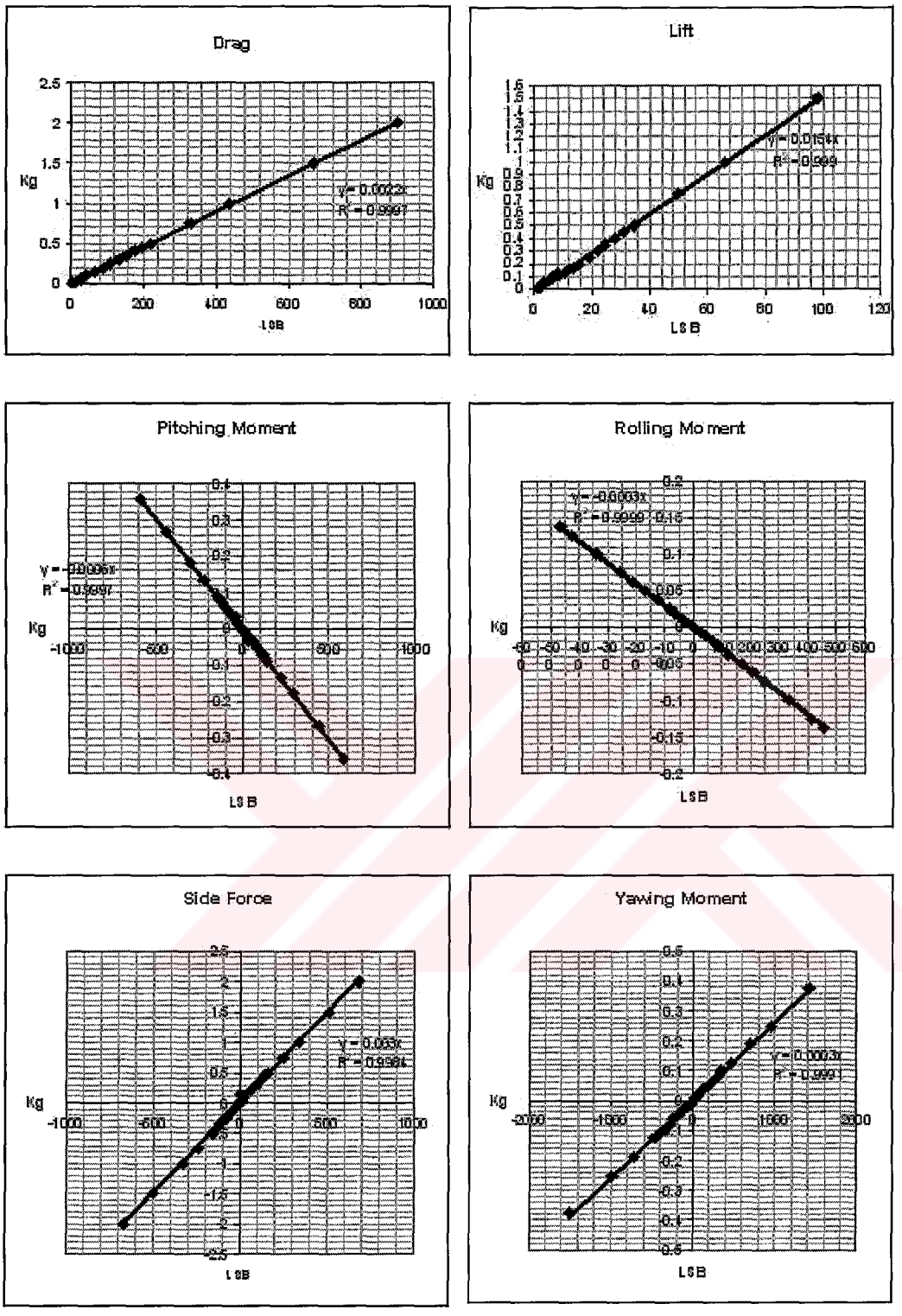

Fig. 3.34 Calibration curves of transducers.

3.6.5.5 Matlab Software

To acquire data a Matlab software is created. This software reads the digit values from the PCL-818H card and multiplies the input with the calibration matrix to give the loads in engineering units.

The software is designed to show and save the read values with time. A scope module is used to visualize the measurement with time. After doing measurements, time-avarages of the values are calculated for each yaw and incidence angle.

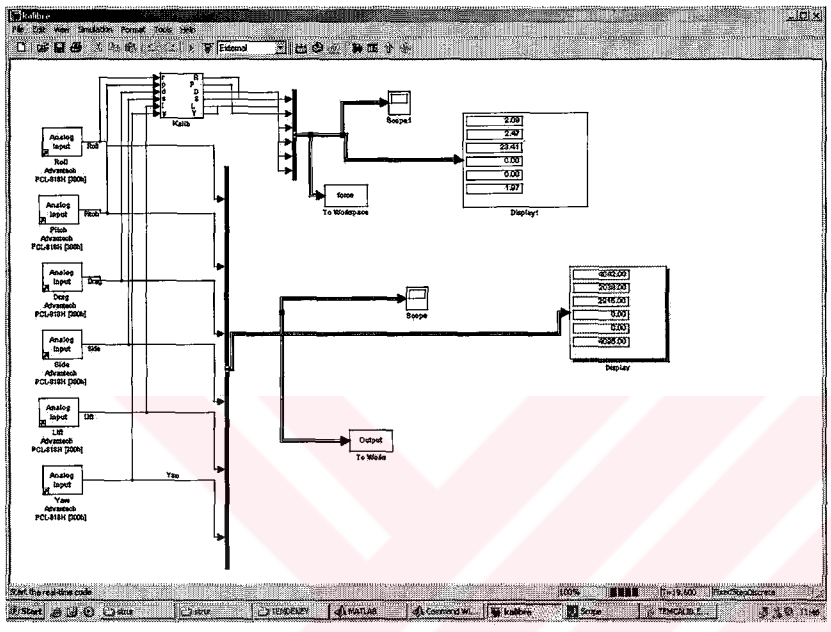

Fig. 3.35 Matlab Software for data acquisition.

Calibration and interaction coefficients are entered to the calibration module by the user.

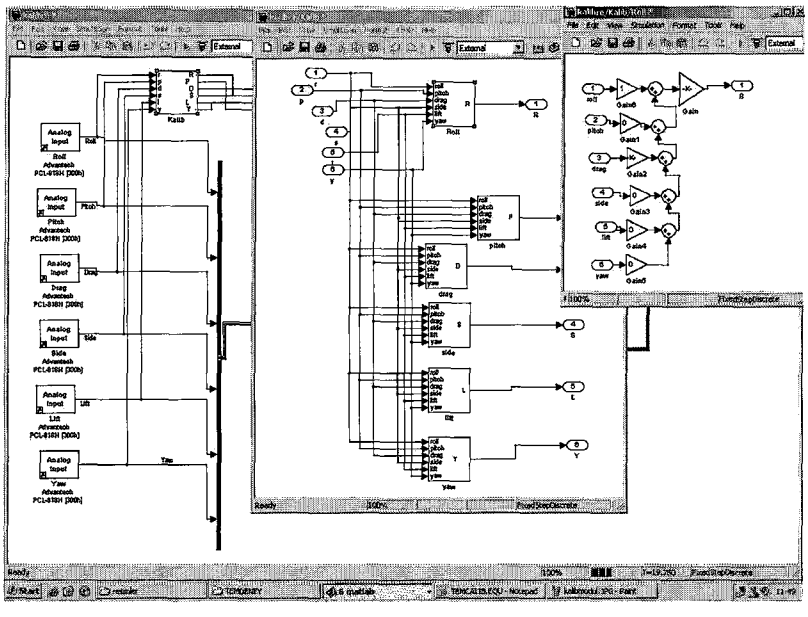

Fig. 3.36 Calibration module in Matlab Software.

3.6.5.6 Assembly of The Models to Balance

Models are assembled to the balance by two main struts and a tail strut. Employing two main struts has been prefered for the sake of yaw and roll moment measurement sensitivity. Pitching moment is measured by the load transferred to the balance by tail strut.

When deciding the main strut lenghts, the criteria was to aligning the tunel centerline and the model centerline. In Fig. 3.37 The length of the main struts are given.

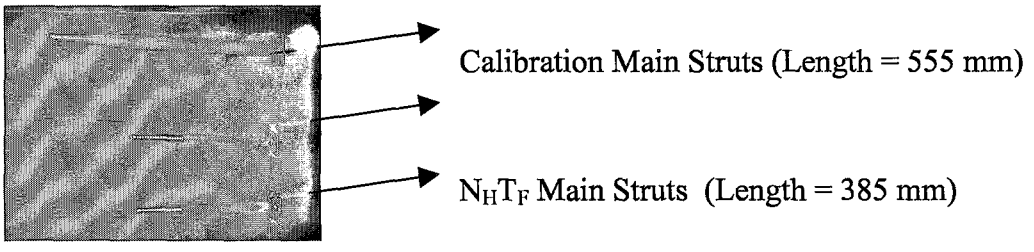

Fig. 3.37 Main Struts.

When assembling the struts to the balance, perpendicularity must be obtained. Otherwise there will be error measuring the lift, rollling and yawing moments.

The base platforms of the main struts should be bolted to the balance tightly to prevent vibrations. Pictures are given in Figures 3.38 to illustrate the connections of struts to the balance.

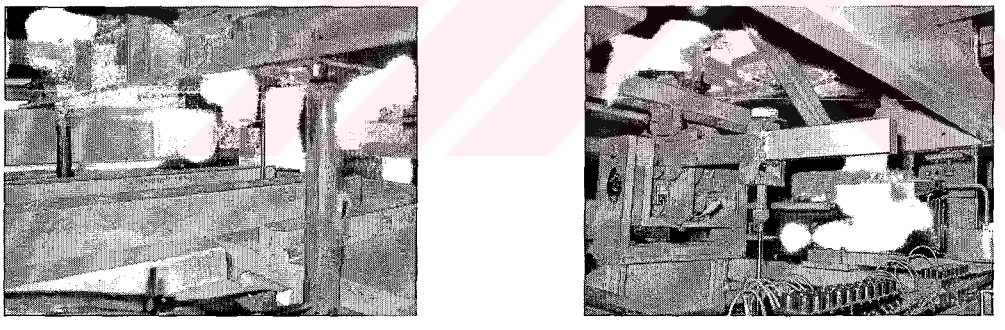

Fig. 3.38 Connection of main and tail strut to the balance.

Models are assembled to a horizontal bar to pitch freely for accurate measurement of pitching moment. This horizontal bar is then assemled to the main struts. Tail strut is connected to cowl region of the model. Pictures are given in Fig 3.39 to illustrate connection of horizontal bar and tail strut.

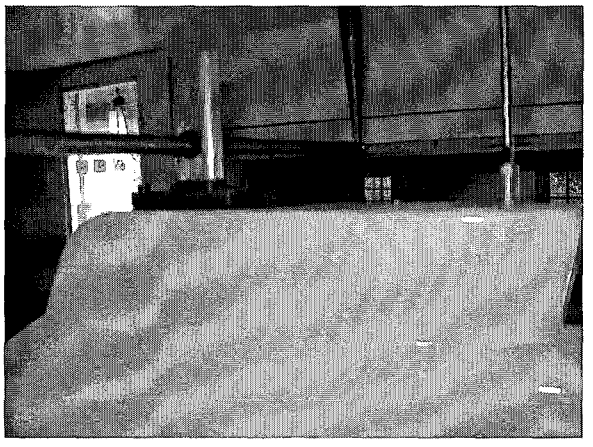

Fig. 3.39 Connection of horizontal bar to model and main struts and tail strut.

For vibration damping, truss system made of aliminum bars are employed in N_DT_E configuration model and plexiglass plates are employed in N_HT_F configuration model. Pictures of these structures are given in Fig 3.40.

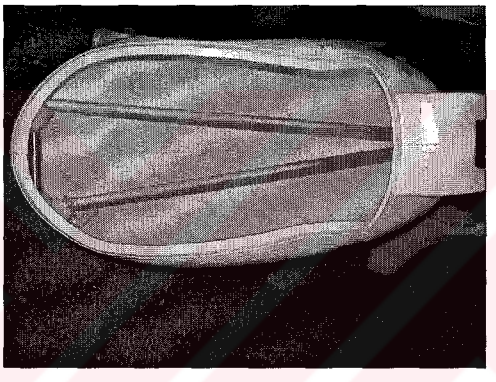

Fig. 3.40.a Aluminum truss structure for N_DT_E configuration model .

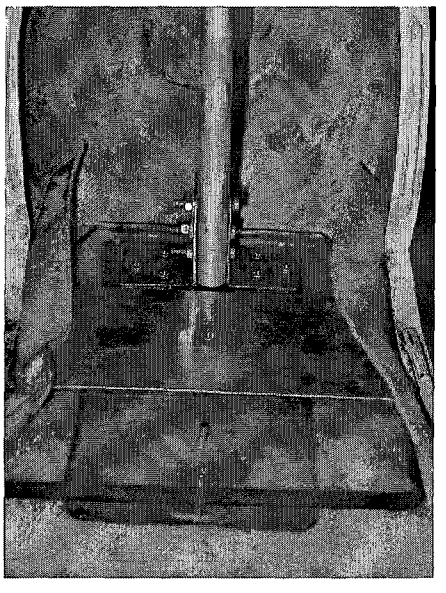

Fig. 3.40.b Plexiglas plates for N_HT_F configuration model.

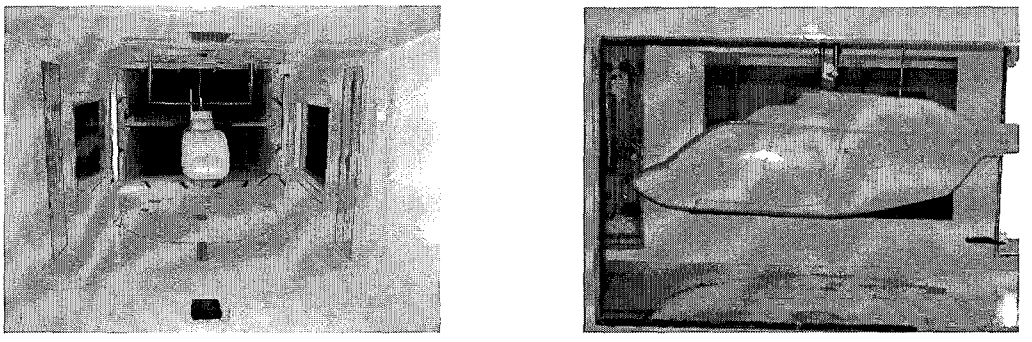

Fig. 3.41 Placement of N_HT_F configuration model in tunnel.

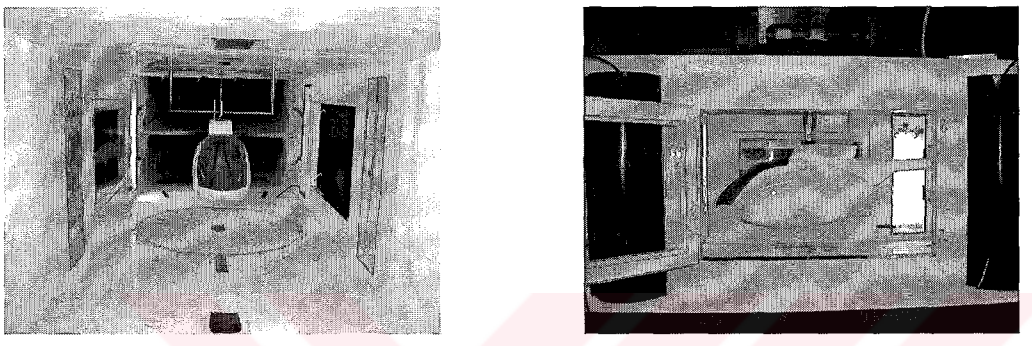

Fig. 3.42 Placement of N_DT_E configuration model in tunnel.

3.6.5.7 Test Setup and Procedure

The models are aligned with the tunnel test section centerline. The tunnel airspeed has been chosen 20 m/s to obtain the Reynolds number of $Re_l = 2.0925x10^6$ for N_HT_F configuration model and $Re_l = 1.9511x10^6$ for N_DT_E configuration model. Reynolds number selection has been done according to the historical background of helicopter fuselage balance measurements. Dynamic pressure corresponding to this speed is 25 mmH_2O.

Sideslip angle was changed from –16 to 16 degrees at incidence angle values of –5, 0, 5, 10, 15. First, incidence angle of the model had been adjusted and then sideslip angle was changed. Zero measurements were done at each sideslip angle by setting the tunnel speed to zero for eliminating the gravitational loads. After zero measurements, tunnel speed was set to 20 m/s to measure the aerodynamic loads.

3.6.5.8 Sign Convention and Data Correction

Positive direction of the measured components are, lift in upwards direction, drag in backwards direction , sideforce in left side direction, rolling moment forcing the right side of the model down, pitching moment is forcing the model nose up and yawing moment is forcing the model heading left. Sideslip angle is positive when the

model is heading right and incidence angle is positive in nose up direction (Fig. 3.43).

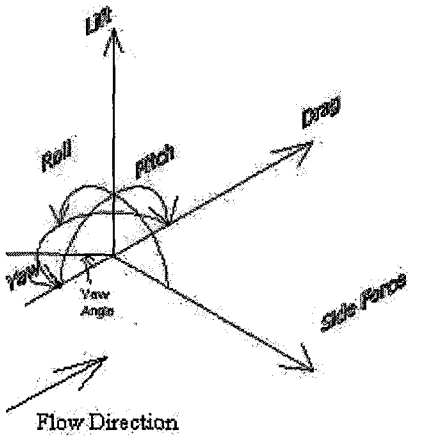

Fig. 3.43 Positive directions of the load components and sideslip angle.

Strut effects were eliminated by substracting the model off strut experiment results from the model on results.

Moment values are altered in that they were transferred from resolving centre of the balance to pivot point of the hub. All force and moment components transformed from balance coordinates which yaws with model but doesn't pitch, to flow coordinates which doesn't yaw nor pitch with the model and is parallel to tunnel walls.

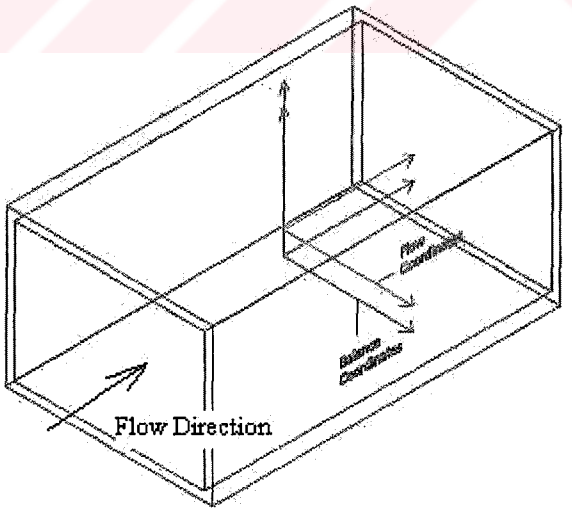

Fig. 3.44 Coordinate Systems.

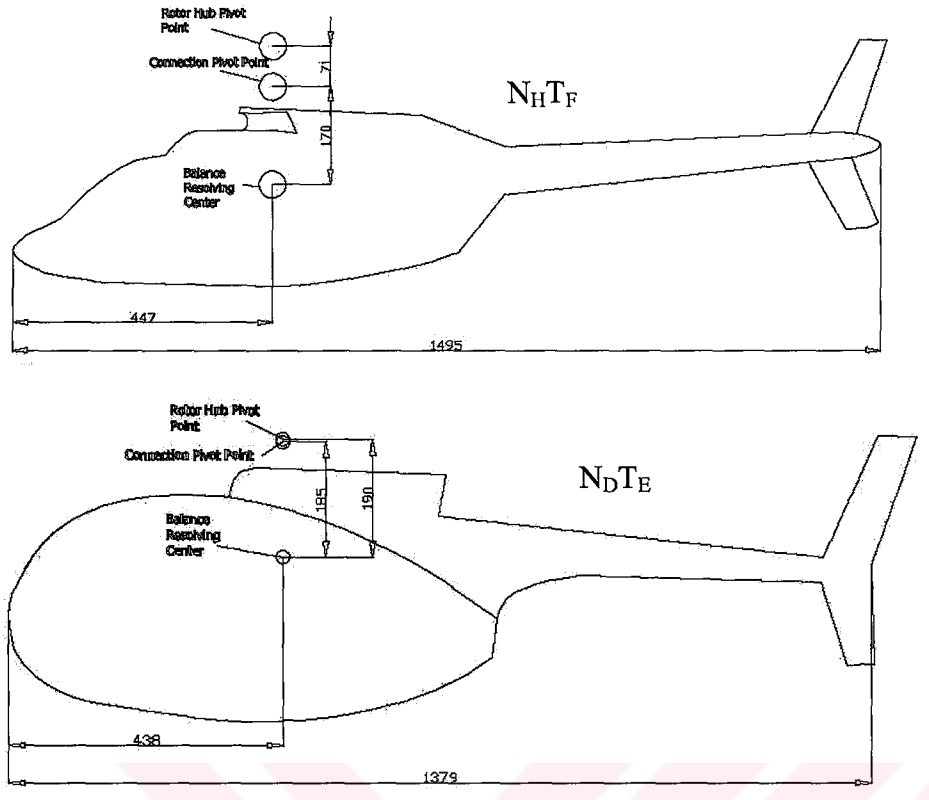

Fig. 3.45 Location of Rotor Hub Pivot Point for both models.

4. RESULTS AND DISCUSSIONS

4.1. Introduction

In this chapter, the flow visualization images, CTA measurement results of N_HT_F configuration model and force and moment aerodynamic characteristics of N_HT_F configuration and N_DT_E configuration models are given.

4.2. Flow Around Helicopter Fuselage Without Rotor

4.2.1. Qualitative Flow Visualization Experiments

The main interest of this study is the flow in the forebody region of the fuselage. According to the juncture regions, the front part of the fuselage has been divided into four regions. These are nose, nose-cabin junction, cabin-cowl junction and cowl regions (Fig. 4.1). Oil film visualization experiments have been accomplished at the fuselage incidence of 0^0, 10^0 and -5^0 at 0^0 of sideslip angle and 15^0 of sideslip angle at 0^0 of incidence angle. Smoke flow experiments have been accomplished at 0^0 and 10^0 of incidence angle. The free-stream velocity is 20 m/s for oil film visualization and 5 m/s for smoke flow visualization.

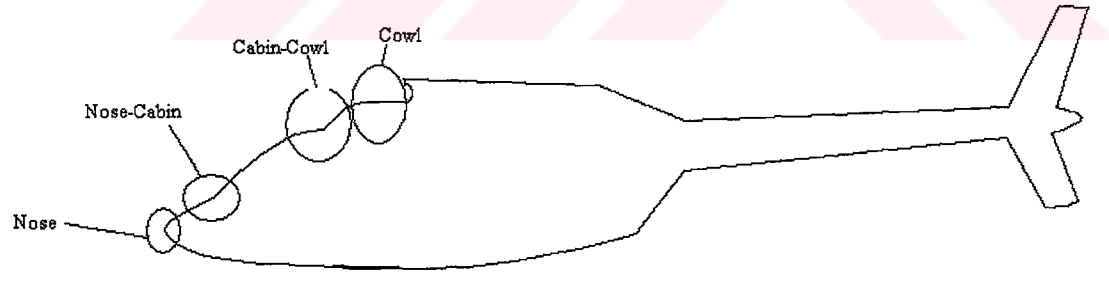

Fig. 4.1 Regions of interest.

The pictures captured from the visualization techniques are given together for nose region in Fig. 4.2.a for 0^0 of incidence, in Fig. 4.2.b for 10^0 of incidence and 4.2.c for -5^0 of incidence. For the smoke images the flow direction is from right to left. The main features of the surface streamlines observed from images have been also sketched in the same figure. As it is observed from the images that an attachment node (see Fig. 2.10) occurs in the observed area corresponds to stagnation point line. Positive incidence of the fuselage causes a deformation of the field and attachment node move towards the lower surface.

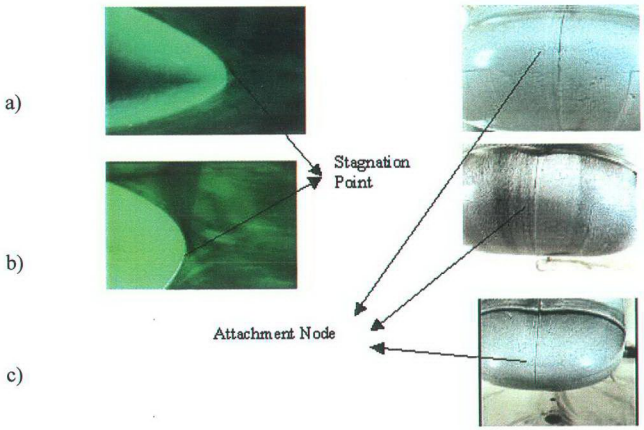

Fig. 4.2 Flow Visualization images for the nose region for -5^0, 0^0 and 10^0 of incidence.

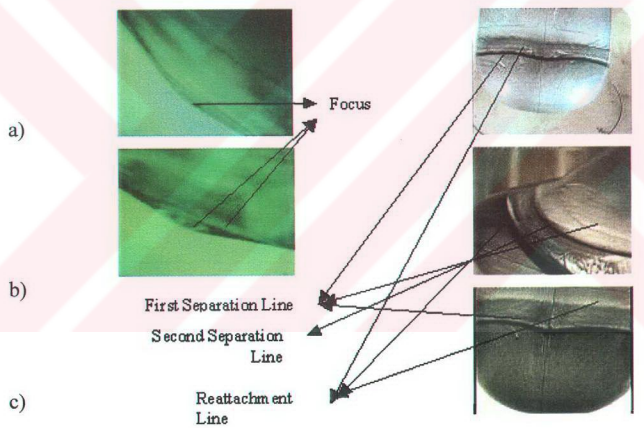

Fig. 4.3 Flow Visualization images for the nose-cabin junction region for -5^0, 0^0 and 10^0 of incidence.

Images for nose- cabin junction region are given together in Fig. 4.3.a for 0^0 of incidence, in Fig. 4.3.b for 10^0 of incidence and in Fig.4.3.c for -5^0 of incidence. As it is seen from the figures that, the flow leaves the surface of the body (separates) along a singular line and reattaches to surface along another singular line. These lines are separation and attachment lines (see Fig. 2.16 and 2.17). For 10^0 of incidence, there are two oil-accumulated lines, which correspond to separation lines. At the cabin surface reattachment occurs and this corresponds to bubble type separation from two-dimensional point of view. From the smoke flow visualization images; it is

observed that two foci have been formed in the separation bubble for 10^0 and one focus for 0^0 of incidence. This has been revealed by oil film visualization images. One oil accumulated line for 0^0 of incidence and two oil accumulated line for 10^0 of incidence. From three-dimensional point of view, it is observed that horseshoe vortex with one focus for 0^0 and -5^0 of incidence and with two foci for 10^0 of incidence occurs between separation and reattachment lines. Saddle point and half node point of the structure can be observed in the images (see Fig. 2.16 and 2.17). In addition to these, it has been observed that positive angle of incidence increases the height and the length of the horseshoe vortex.

Images for cabin- cowl junction region are given together in Fig. 4.4.a for 0^0 of incidence, in Fig. 4.4.b for 10^0 of incidence and in Fig.4.4.c for -5^0 of incidence. There are two oil-accumulated lines, which correspond to separation lines. At the cabin-cowl junction surface, a reattachment line occurs similarly with the nose-cabin junction. From two-dimensional point of view from smoke flow images, there are two foci in the separation bubble for 0^0 of incidence and for 10^0 of incidence revealing the oil film visualization images. From three-dimensional point of view, horseshoe vortex that occurs in this region has two foci. Again saddle point and half node of the separation and attachment is observed in the images. It is also observed that height and length of the horseshoe vortex increase with increasing angle of incidence.

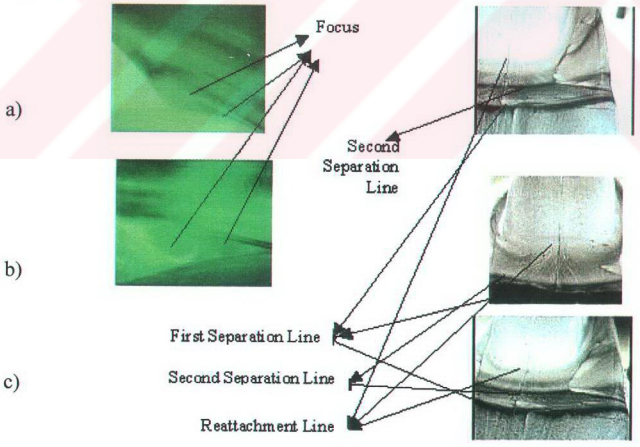

Fig. 4.4 Flow Visualization images for the cabin-cowl junction region for -5^0, 0^0 and 10^0 of incidence.

Images for cowl region are given together in Fig. 4.5.a for 0^0 of incidence, in Fig. 4.5.b for 10^0 of incidence and in Fig.4.5.c for -5^0 of incidence. There are again two

oil-accumulated lines, which correspond to separation lines for both angles of incidence. From two-dimensional view of smoke flow images, separated flow reattaches at the cowl surface and a separation bubble with two foci occurs for both angles of incidence revealing the oil film visualization images. From three-dimensional point of view of oil film visualization images, horseshoe vortex with two foci is observed between the separation and reattachment lines.

The region of reversed flow grows in extent as angle of incidence increases. For -5^0, 0^0 and 10^0 angles of incidence, the flow separated from the surface at nose- cabin, cabin-cowl junction and cowl regions reattaches to the surface and form separation bubble at the symmetry plane of the fuselage forming horseshoe vortices beneath the surface.

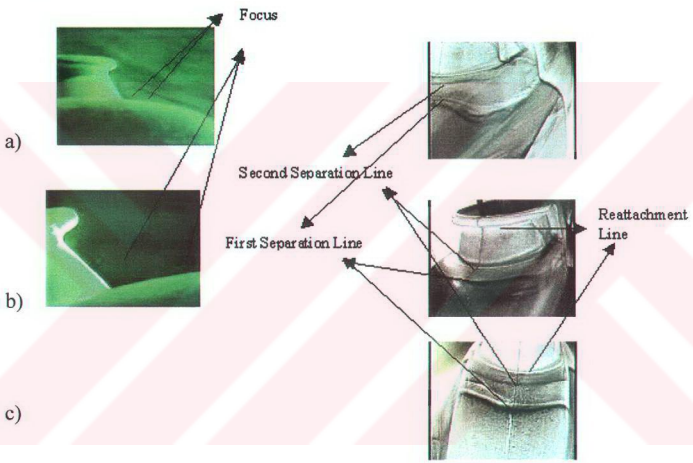

Fig. 4.5 Flow Visualization images for the cabin-cowl junction region for -5^0, 0^0 and 10^0 of incidence.

To see the sideslip angle effect on the surface flow of helicopter fuselage, images for 15^0 (heading right) of sideslip with 0^0 of incidence are given in Fig. 4.6.a for nose-cabin junction, Fig.4.6.b for cabin-cowl junction and Fig.4.6.c for cowl region.

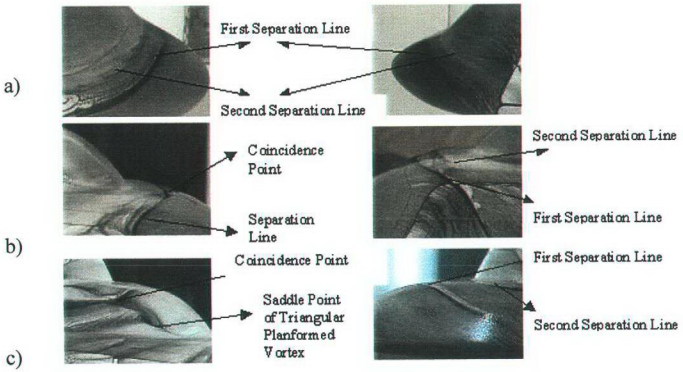

Fig. 4.6 Flow Visualization images for -5^0 of sideslip angle for nose-cabin, cabin-cowl and cowl regions.

From the Fig. 4.6.a for nose-cabin junction region, one separation and one reattachment lines are observed which means horseshoe vortex has one focus. Saddle point of the horseshoe vortex, occurs on the left side of the model centerline.

For the cabin-cowl junction region (Fig. 4.6.b), there exist two separation lines on the left side of the model centerline coinciding to form one separation line to the right of the centerline. On the left side of the model, horseshoe vortex has two foci. The second focus grows larger and become one focus to the right of the model centerline. The saddle point of separation remains on the left side of the model.

For the cowl region (Fig. 4.6.c), two separation lines exist on the left side of the model centerline, which means horseshoe vortex, has two foci. On the right side of the centerline, a triangular planformed horseshoe vortex exists. This triangular planform horseshoe vortex coincides with the separation lines coming from the left side of the model centerline and forms complex structured vortices on the right side of the cowl region.

4.2.2. Quantitative Flow Measurements

The magnitude of velocities has been measured by CTA on the longitudunal center section of the forebody region. Velocity magnitude contours are given in Fig. 4.7, 4.8 and 4.9 for incidence angles of -10^0, 0^0 and 10^0 respectively. As indicated in the flow visualization experiment results, the separation dimensions in the junction regions are visible. Positive angle of incidence increases and negative angle of incidence decreases the low velocity region dimensions on the upper part of the forebody.

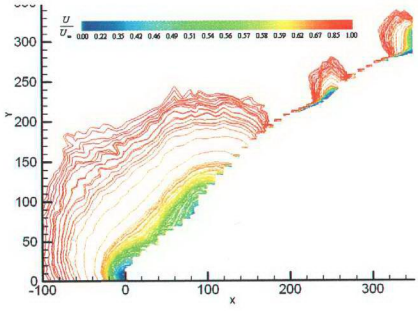

Fig. 4.7 Velocity magnitude contours for incidence angle of -10^0 .

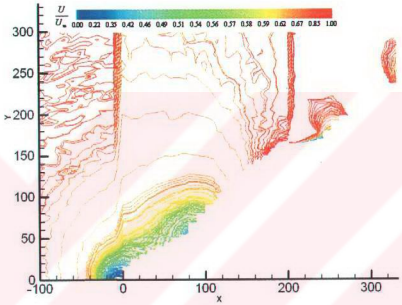

Fig. 4.8 Velocity magnitude contours for incidence angle of 0^0.

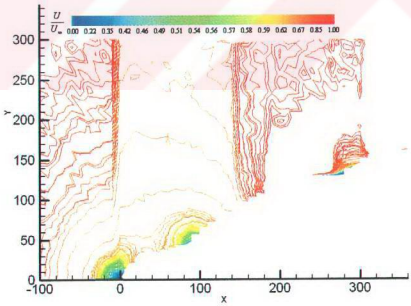

Fig. 4.9 Velocity magnitude contours for incidence angle of 10^0.

4.3. Force and Moment Characteristics of Isolated Helicopter Fuselage

The objective is to determine the effect of fuselage shape on the aerodynamic characteristics experimentally. The tests were performed at free stream velocity of 20 m/s, which corresponds to Reynolds number of 2.0925x106 for NHTF and 1.9511x106 for NDTE configuration models based on overall fuselage lengths. Tests were conducted with and without horizontal stabilizers. Location and geometry of the horizontal stabilizers are given in APP. C.

Reference areas and lengths are assumed according to [20]. Horizontal projected area (S_P) is taken reference for Pitching moment (C_m), drag (C_D), lift (C_L) and side-forces (C_Y) as reference area. Side projected area (S_S) is taken reference for rolling (C_l) and yawing (C_n) moments as reference area. Fuselage length is taken reference for all coefficients as reference length.

Drag and lift coefficients are given for the angles of incidence between –5 and 15 degrees in Fig. 4.10 and 4.11 for N_HT_F configuration model. These results are presented fuselage alone and for fuselage with horizontal stabilizers. Lift coefficient increases with angle of incidence for fuselage alone and with horizontal stabilizers conditions and stabilizers cause increase in the slope of the lift curve. Drag coefficient decreases with angle of incidence for fuselage alone condition. This can be explained by the results founded by the flow visualization experiments that the positive increase in the angle of incidence increases the vortex dimensions on the upper region of the fuselage but decreases the vortex dimensions on rear upswept region. With the horizontal stabilizers installed, C_D has a parabolic distribution with a minimum value of 0.085 at 7^0 angle of incidence.

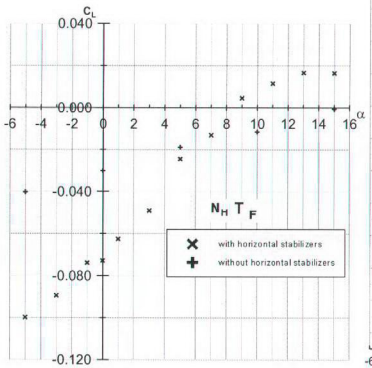

Fig. 4.10 C_L distribution of $N_H T_F$ configuration.

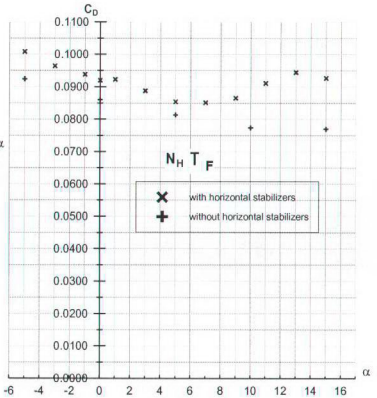

Fig. 4.11 CD distribution of NHTF configuration.

To determine the longitudinal stability characteristics of the fuselage alone, pitching moment coefficient variation is given in Fig. 4.12. As it is seen from the figure, for the fuselage alone configuration negative (nose down) pitching moment coefficient increases as the incidence angle decreases. This positive slope means that $N_H T_F$ configuration fuselage does not satisfy the static longitudinal stability condition. By using horizontal stabilizers, the slope of the C_m has positive value in the region of incidence angle $-4<\alpha<0$ and $10<\alpha<15$. But it has negative slope region of $0<\alpha<10$, which satisfies the longitudinal stability condition.

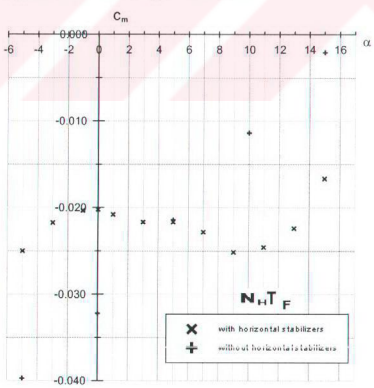

Fig. 4.12 C_m distribution of $N_H T_F$ configuration.

Drag coefficient distribution with sideslip angle for different angles of incidence is given in Fig. 4.13.a. The drag coefficient has minimum values at approximately –2

sideslip angle. For the sideslip angles 10, drag coefficient decreases with increasing angle of incidence. After 10^0 of sideslip angle, the angle of incidence does not affect the drag coefficient distribution. Horizontal stabilizers does not effect the C_D distribution with sideslip angle significantly as seen in Fig. 4.13.b.

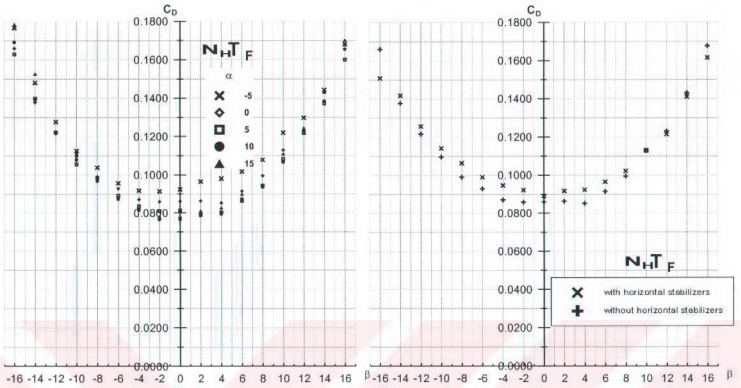

Fig. 4.13 a) C_D distribution with β. **b)** C_D distribution with β at 0^0 of incidence.

The lift coefficient distribution has two linear region with negative slope from 0 to 8 and 8 to 16 of side slip as seen in Fig. 4.14.a. Horizontal stabilizers cause increase in the downforce especially in the first region as seen in Fig. 4.14.b.

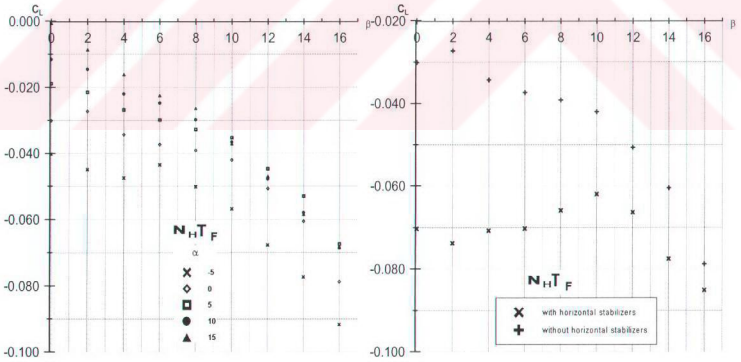

Fig. 4.14 a) C_L distribution with β. **b)** C_L distribution with β at 0^0 of incidence.

Figures 4.15.a and b show that the side-force coefficient changes linearly with sideslip angle and has a negative slope. The increase in the angle of incidence increases the slope of the curve. The horizontal stabilizers do not affect the side-force distribution.

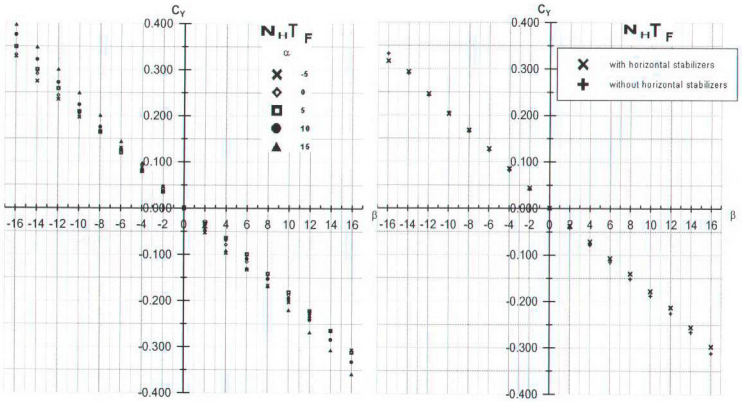

Fig. 4.15 a) C_Y distribution with β. **b)** C_Y distribution with β at 0^0 of incidence.

The pitching moment coefficient increases in negative direction (nose down) with increasing sideslip angle and decreases in negative direction with increasing angle of incidence as seen in Fig. 4.16.a. Horizontal stabilizers cause decrease in the pitching moment coefficient as seen in Fig. 4.16.b.

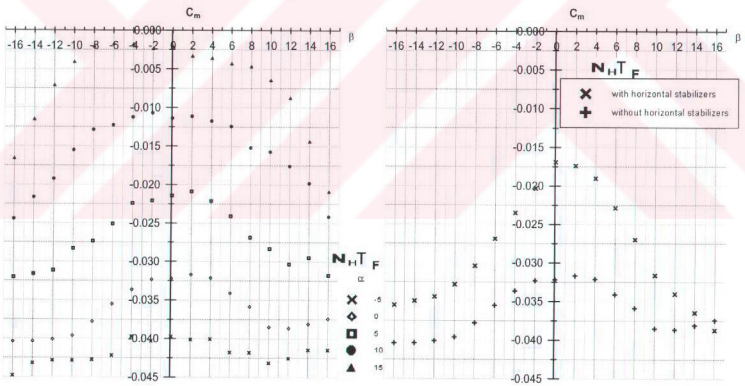

Fig. 4.16 a) C_m distribution with β. **b)** C_m distribution with β at 0^0 of incidence.

In order to determine the directional and rolling stability characteristics of the N_HT_F fuselage alone, the variation of moment coefficients with the sideslip angle was examined.

Yawing moment variation with sideslip angle is given in Fig. 4.17.a. These results show that fuselage alone has a positive slope, which satisfies the static directional

stability condition the angle of incidences of α=-5^0, 0^0 and 15^0, and at α=5^0 and 10^0 for sideslip angle values greater than ±6^0. The magnitude of the directional stability decreases with increasing angle of incidence. With horizontal stabilizers installed, the slope of the curve decreases as seen in Fig.4.17.b.

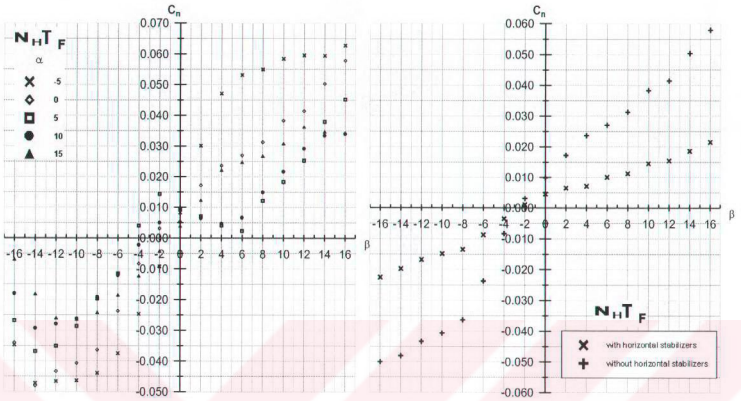

Fig. 4.17 a) C_n distribution with β. **b)** C_n distribution with β at 0^0 of incidence.

Rolling moment variation with sideslip angle is given in Fig. 4.18.a. These results show that fuselage alone has a negative slope, which means stable for rolling motion for the selected range of incidence angles. The magnitude of the rolling moment increases with the increasing incidence angle. Horizontal stabilizers do not affect the rolling moment coefficient distribution with sideslip angle significantly as seen in Fig. 4.18.b.

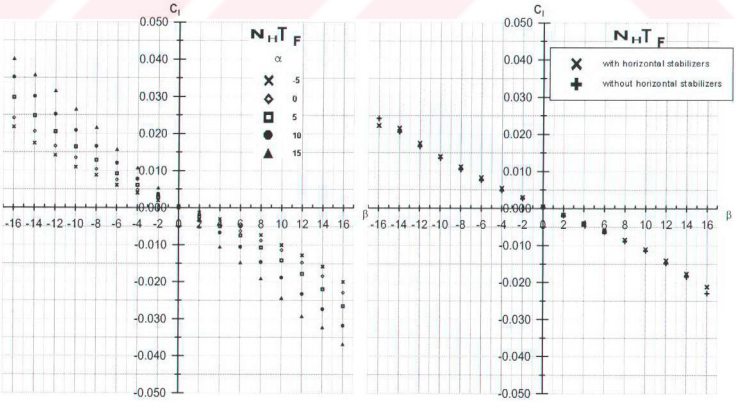

Fig. 4.18 a) C_l distribution with β. **b)** C_l distribution with β at 0^0 of incidence.

4.3.1. Comparison of Force and Moment Characteristics of N_HT_F and N_DT_E Configurations

In this section comparison of N_HT_F and N_DT_E fuselage configurations will be given. Force and moment coefficient graphs will be given together to be compared.

Drag and lift coefficients are given for the incidence angles between –5 and 15 in Fig. 4.19 and 4.20 respectively. Examination of the data indicates that

- Drag coefficient of N_HT_F configuration is smaller than the N_DT_E configuration.
- Lift coefficient of N_HT_F configuration is greater than the N_DT_E configuration.

This result shows that the N_HT_F configuration has better drag and lift values for the selected incidence angle region.

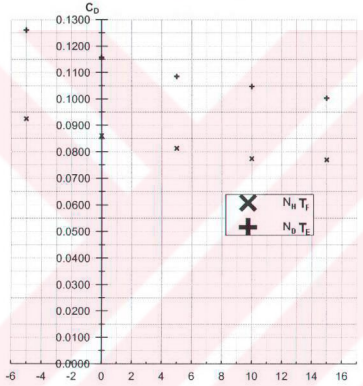

Fig. 4.19 C_D comparison of N_HT_F and N_DT_E configurations.

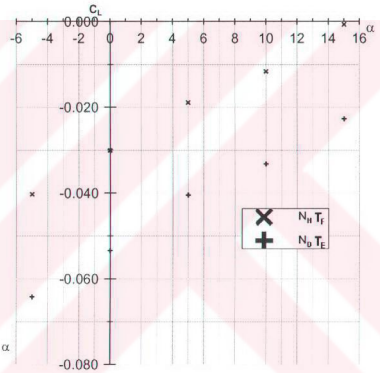

Fig. 4.20 C_L comparison of N_HT_F and N_DT_E configurations.

The longitudinal stability characteristic of the N_HT_F configuration is better than N_DT_E configuration as seen in Fig. 4.21. C_m of both configurations decreases with increasing incidence angle, but N_DT_E configuration has always greater negative pitching moment (nose down) for a specific incidence angle.

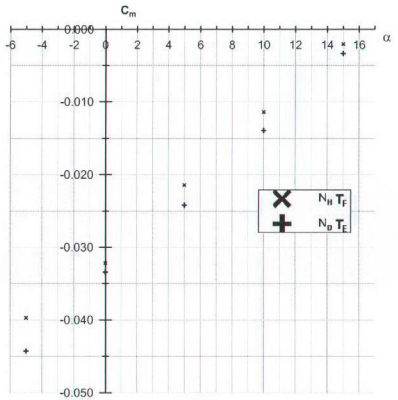

Fig. 4.21 C_m comparison of N_HT_F and N_DT_E configurations.

The drag coefficient distribution with sideslip angle for different values of incidence angles is shown in Fig. 4.22. Drag coefficient increase with sideslip angle of N_DT_E configuration is greater than N_HT_F configuration.

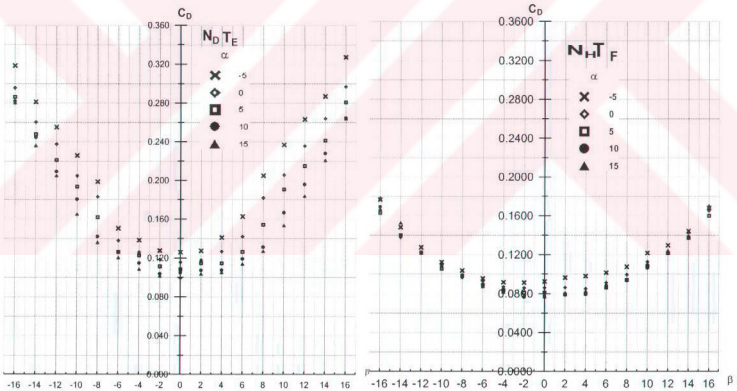

Fig. 4.22 C_D distribution with sideslip angle of N_HT_F and N_DT_E configurations.

N_HT_F Configuration has smaller negative lift values, which means less download as seen in Fig. 4.23. Lift coefficient increase in negative direction with sideslip angle of N_DT_E configuration is greater values than N_HT_F configuration.

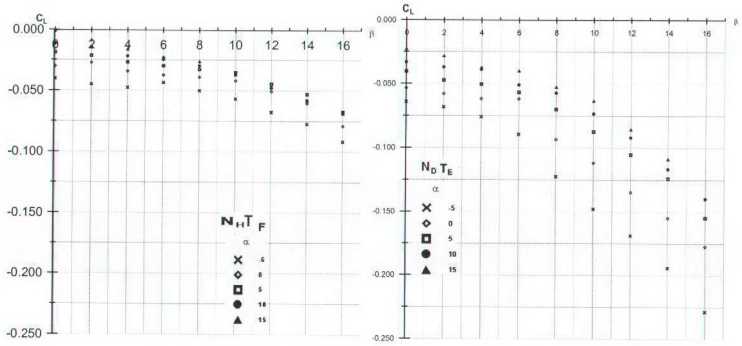

Fig. 4.23 C_L distribution with sideslip angle of $N_H T_F$ and $N_D T_E$ configurations.

Fig. 4.24 shows that there is no significant change in side-force with angle of incidence for both configurations. Also both configurations have approximately the same C_Y curve slopes. Side force magnitudes increase linearly with increasing sideslip angle for both configurations.

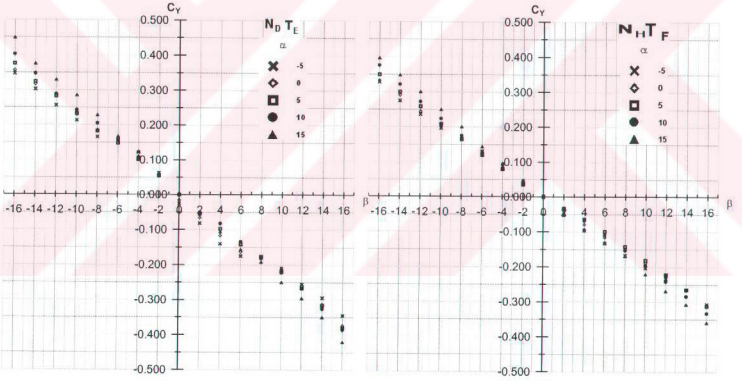

Fig. 4.24 C_Y distribution with sideslip angle of $N_H T_F$ and $N_D T_E$ configurations.

Magnitude of C_m increases in nose down direction with increasing magnitude of sideslip angle for both configurations. But increase in magnitude of C_m with sideslip angle for $N_D T_E$ configuration is greater then $N_H T_F$ configuration as seen in Fig.4.25.

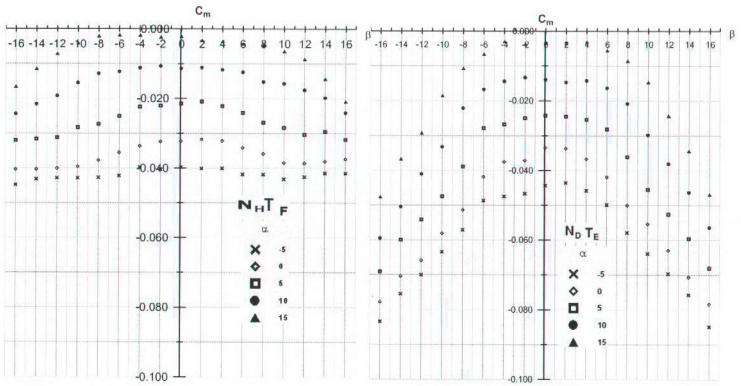

Fig. 4.25 C_m distribution with sideslip angle of N_HT_F and N_DT_E configurations.

C_n distribution with sideslip angle is given for both models in Fig. 4.26. As seen in figures, N_HT_F model has better directional stability than N_DT_E model. N_DT_E model is directionally stable only for -5^0 of incidence angle condition. In other situations, model is directionally unstable.

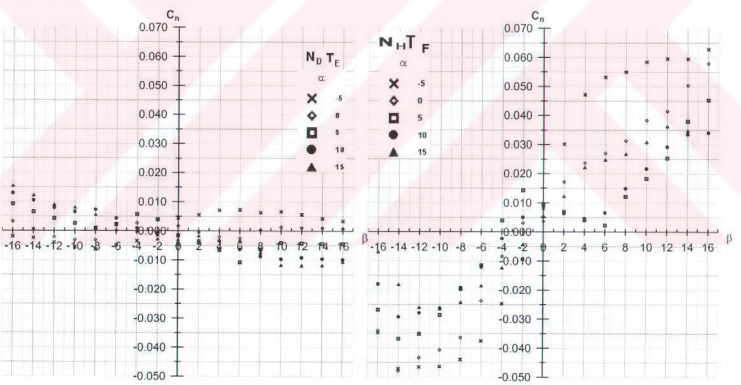

Fig. 4.26 C_n distribution with sideslip angle of N_HT_F and N_DT_E configurations.

C_l distribution with sideslip angle is given for both models in Fig. 4.27. as seen in figures, both models have negative slope which means they are both stable for rolling motion. N_DT_E model is more stable for rolling motion, since it has greater C_l slope than N_HT_F model.

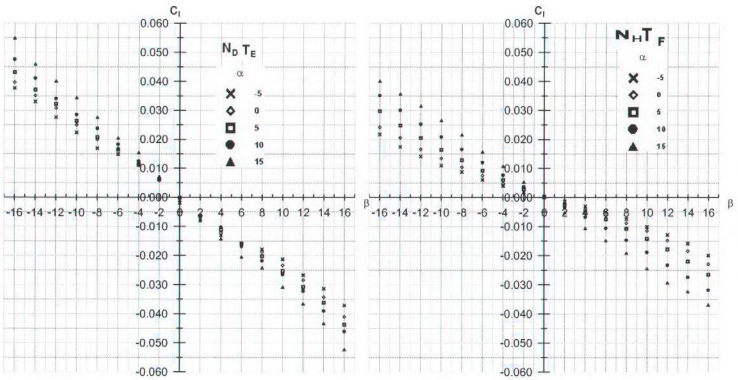

Fig. 4.27 C_l distribution with sideslip angle of N_HT_F and N_DT_E configurations.

4.3.2. Effect of Horizontal Stabilizers on aerodynamic characteristics of N_DT_E Configuration Model

In this section, the effect of horizontal stabilizers on the force and moment characteristics of N_DT_E configuration model will be given. Location and geometry of the horizontal stabilizers are given in APP. C.

Drag and lift coefficients distributions with angle of incidence are given for the fuselage alone and with the horizontal stabilizers installed in figures 4.28 and 4.29 respectively.

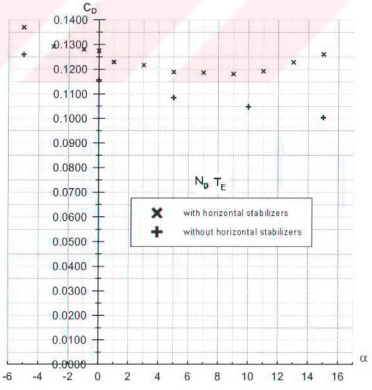

Fig. 4.28 C_D distribution of N_DT_E configuration with and without horizontal stabilizers with incidence angle.

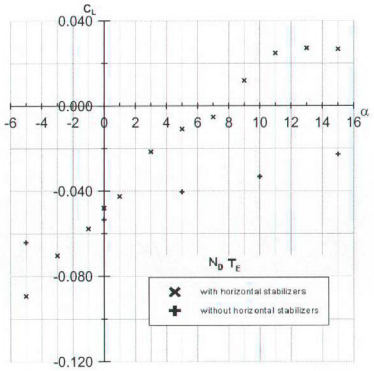

Fig. 4.29 C_L distribution of N_DT_E configuration with and without horizontal stabilizers with incidence angle.

With horizontal stabilizers installed, drag coefficient distribution with incidence angle has a parabolic behavior, which has a minimum value of 0.116 at 9^0 of incidence. The lift distribution has a greater slope with the horizontal stabilizers installed than the condition horizontal stabilizers not installed.

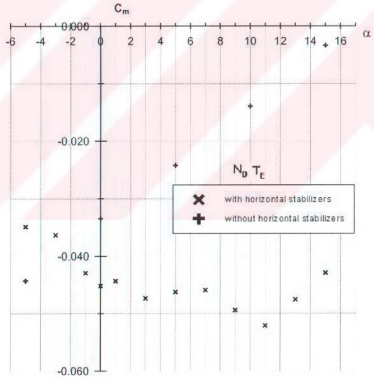

Fig. 4.30 C_m distribution of N_DT_E configuration with and without horizontal stabilizers with incidence angle.

It is founded for the fuselage alone conditions that the N_DT_E configuration fuselage has a negative contribution to static longitudinal stability. With horizontal stabilizers installed, the slope of the pitching moment coefficient has negative value in the region of incidence angle $-5^0<\alpha<11^0$, which means a positive contribution to static longitudinal stability as seen in Fig.4.30.

The drag coefficient distribution with sideslip angle with and without the horizontal stabilizers installed is shown in Fig. 4.31. Horizontal stabilizers do not affect the drag coefficient distribution behavior significantly, but cause a small increase.

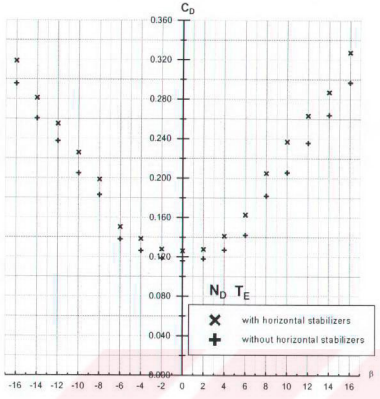

Fig. 4.31 C_D distribution of N_DT_E configuration with and without horizontal stabilizers with sideslip angle.

Horizontal stabilizers do not affect the C_L distribution with sideslip angle significantly as seen in figure 4.32.

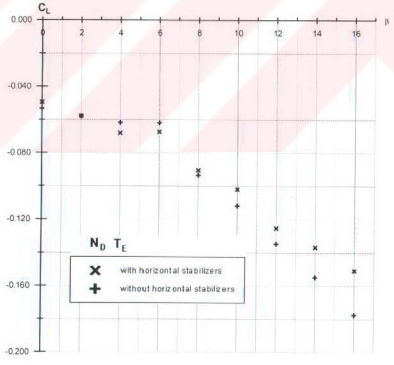

Fig. 4.32 C_L distribution of N_DT_E configuration with and without horizontal stabilizers with sideslip angle.

Fig. 4.33 shows that there is no significant change in sideforce distribution with sideslip angle with and without horizontal stabilizers.

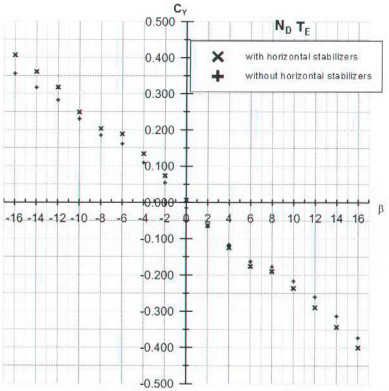

Fig. 4.33 C_Y distribution of $N_D T_E$ configuration with and without horizontal stabilizers with sideslip angle.

The horizontal stabilizers do not affect the C_m distribution for sideslip angles greater 6^0 as seen in Fig.4.34. But, for the sideslip angle smaller than 6^0, horizontal stabilizers cause increase in the magnitude of the pitching moment coefficient.

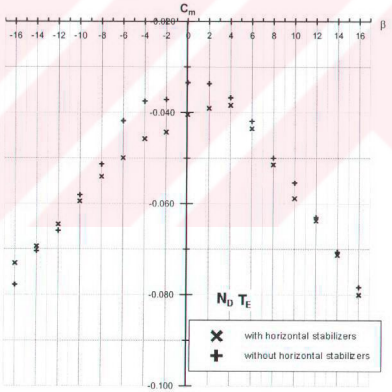

Fig. 4.34 C_m distribution of $N_D T_E$ configuration with and without horizontal stabilizers with sideslip angle.

Fig. 4.35 shows that fuselage with horizontal stabilizer satisfies the static directional stability condition with a positive slope due to the winglets installed on the tips of the stabilizer.

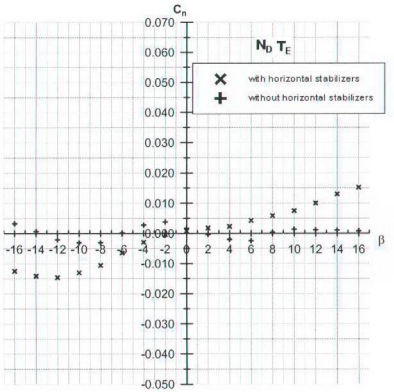

Fig. 4.35 C_n distribution of $N_D T_E$ configuration with and without horizontal stabilizers with sideslip angle.

C_l distribution with sideslip angle is given for $N_D T_E$ model with and without horizontal stabilizer in Fig. 4.36. As seen in figure both configuration has negative slope which means that they are both stable for rolling motion. Fuselage without horizontal stabilizer is more stable for rolling motion, since it has greater C_l slope.

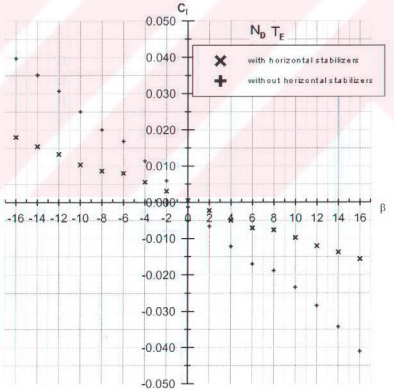

Fig. 4.36 C_l distribution of $N_D T_E$ configuration with and without horizontal stabilizers with sideslip angle.

5. CONCLUSION

Wind tunnel investigation of to determine and compare the aerodynamic characteristics of two different configuration helicopter fuselage shape. The test results have provided the following conclusions:

- Horseshoe vortices occur at the juncture regions of the forebody of the fuselage
- Positive incidence angle increase makes horseshoe vortices grow.
- Sideslip angle makes the structure of the horseshoe vortices more complex.
- Increase in incidence angle increases the upper surface separation vortex dimensions but decreases the separation vortex dimensions on the rear upswept region.

From the results of force and moment measurements for fuselage alone condition, the following conclusions are reached:

- The aft body shape is dominant for the selected incidence angle range.
- N_HT_F configuration fuselage has better drag and lift values for selected sideslip and incidence angle ranges.
- N_HT_F configuration and N_DT_E configuration do not satisfy the static longitudinal stability condition.
- N_HT_F configuration is directionally stable but N_DT_E configuration is unstable.
- N_HT_F configuration and N_DT_E configuration are both satisfying roll stability condition.

From the results of force and moment measurements for fuselage with horizontal stabilizers, the following conclusions are reached:

- With horizontal stabilizers, the magnitude of the negative contribution to the static longitudinal stability decreases for N_HT_F model and especially for N_DT_E model.
- With horizontal stabilizers, the magnitude of the positive contribution to the static directional stability decreases for N_HT_F model. With horizontal stabilizers, N_DT_E model satisfies the static directional stability condition due to the winglets located at the tips of the stabilizer.

- With horizontal stabilizers, the magnitude of positive contribution to the static roll stability decreases for N_DT_E model due to vertical location of the winglets of the stabilizer.

By this study, experimental techniques and procedures are developed for future studies in rotorcraft aerodynamics. This study will constitute basis for future studies. In proceeding studies, effect of different rotorcraft components will be investigated. Rotor effects, different types of horizontal and vertical stabilizers will be tested for these fuselage configurations. The results of this study will guide us to determine the effects of different components on total rotorcraft vehicle.

REFERENCES

[1] **Wilson, F. T. and Ahmed, S. R.**, 1990. Fuselage aerodynamic Design Issues and Rotor/Fuselage Interactional Aerodynamics, AGARD Report , **781,** 4.1-4.38.

[2] **Keys, C. And Wiesner, R.,** 1975. Guidelines for Reducing Helicopter Parasite Drag, 31st AHS Forum, May, Paper No 3 of Rotorcraft Parasite Drag.

[3] **Seddon, J.**, 1982. Aerodynamics of Rear Fuselage Upsweep, 8th ERF.

[4]**Phillipe, J. J.,** 1990. Considerations on Wind Tunnel Tesing Techniques for Rotorcraft, AGARD FDP Special Course, Ankara, Turkey.

[5]**Filipone, A. and Micelsen, J. A.,** 2001. Aerodynamic Drag Prediction of Helicopter Fuselage, Journal of Aircraft, **38**, 326-333

[6] **Delery, J. M.,** 1991. Physics of Vortical Flows.

[7] **Gill, W.,** 1960. Hiller Aircraft Corpration Performance Data Report, No 60-92, 181-281.

[8] **Merzkirch. W. And Gersten, K.,** 1987. Techniques of Flow Visualization, AGARD Report, **302**, 1-93

[9] **Settle, S. G. And Teng, H., Y.,** 1983. Flow Visualization Methods for Separated Three Dimensional Shock Wave/Turbuent Boundary Layer Interactions, AIAA J., **21**, 390-397.

[10] **Maltby, R. L. And Keating, R.F.A.,** 1962. The Surface Oil fil flow Technique for Use in Low Speed Wind Tunnels, AGARD Report, **70**, 29-38.

[11] **Stanbrook, A.**, 1962. The Surface Oil Flow Technique for Use in High Speed Wind Tunnels, AGARD Report, **70**, 39-49.

[12] **Hornung**, H., 1986. Die Entwicklung eines Anstrichbilds bei Windkanalsuchen, THD-Schriftenreihe Wissenschaft und Tecnik, **28**, 113-123.

[13] **Murai, H.; Ihara, A.;Narasakai T.,** 1982. Visual Investigation of Formation Process of Oil-Flow Pattern, The Second International Conferance on Flow Visualization, Hemisphere, Washington, USA.

[14] **Squire, L. C.,** 1962. The motion of Thin Oil Sheet Under The Boundary Layer on a Body, AGARD Report, **70**, 7-28.

[15] **Jorgensen, F., E.,**2002. How to measure turbulence with hot-wire anemometers, Dantec Dynamics.

[16] **Pope, A.**, 1947. Wind Tunnel Testing, pp.95-124, John Wiley & Sons, New York

[17] **TEM Eng. Ltd. Co.,** Balance User Manual

[18] **Adventech Ltd,** 1993. PCL-818H Data Acquisition Card Manual.

[19] **Hasanreisoğlu, A., L.,** 1995. Rüzgar Tünelinde Bilgisayarla Balans Deneyleri, *Yüksek Lisans Tezi*, İTÜ Fen Bilimleri Enstitüsü, İstanbul.

[20] **Wilson, J. C. and Mineck**, R., E., 1975. Wind Tunnel Investigation of Helicopter Rotor Wake Effects on Three Helicopter Fuselage Models, NASA Technical Forum, N75-21249.

APPENDIX A. HELICOPTER FUSELAGE CONFIGURATIONS

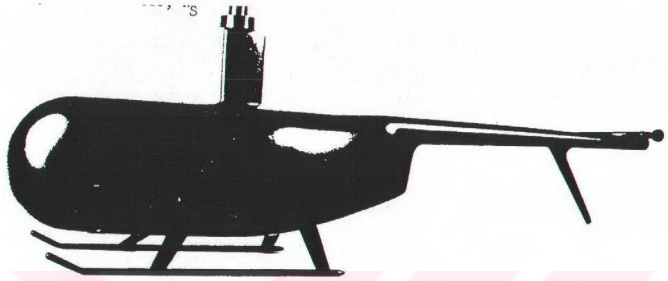

a) Symmetrical Nose, N_S

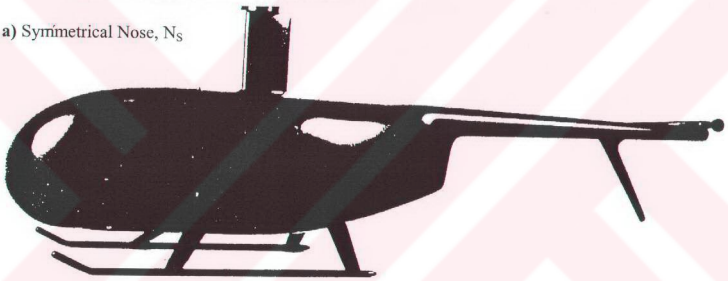

b) Droop Nose, N_D

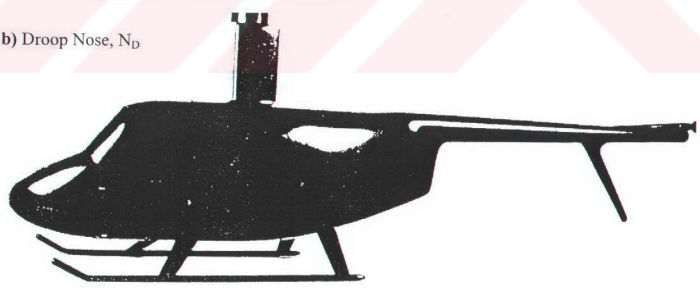

c) Cutback Nose, N_H

Fig. A. 1 Models with High Tail Boom T_F

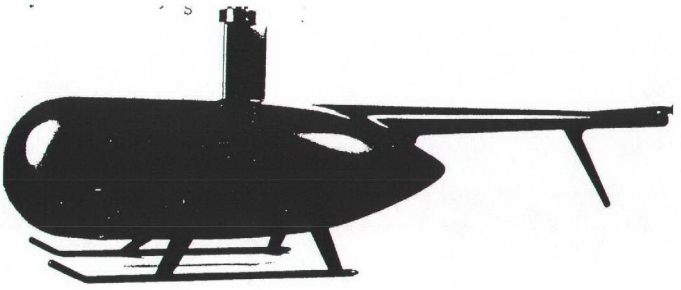

a) Symmetrical Nose, N_S

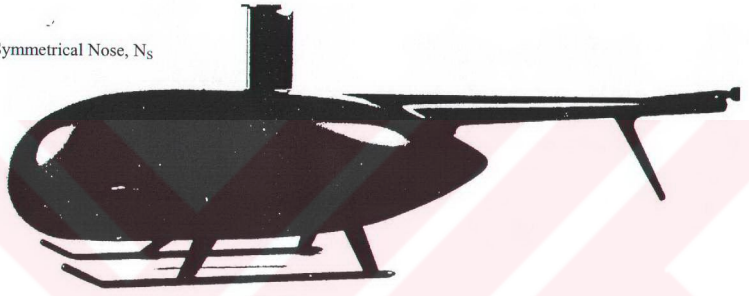

b) Droop Nose, N_D

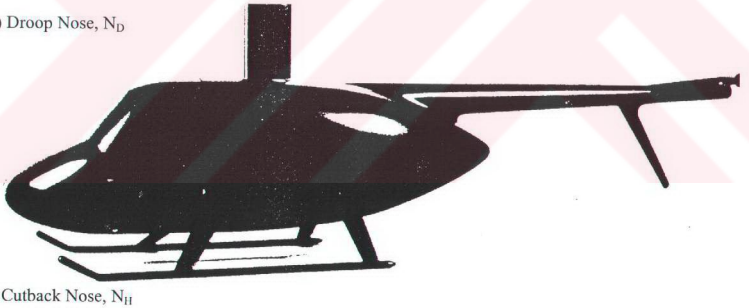

c) Cutback Nose, N_H

Fig. A. 2 Models with High Tail Boom T_E

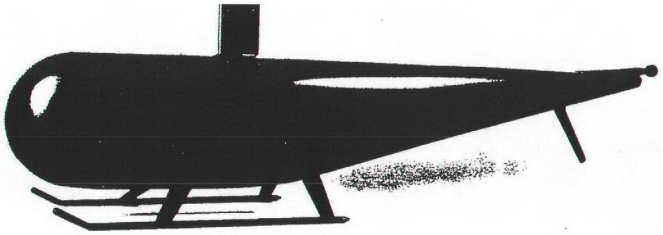

a) Symmetrical Nose, N_S

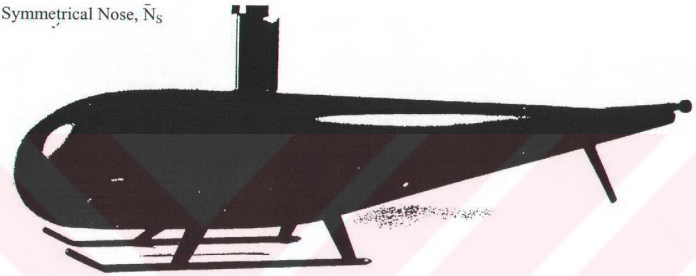

b) Droop Nose, N_D

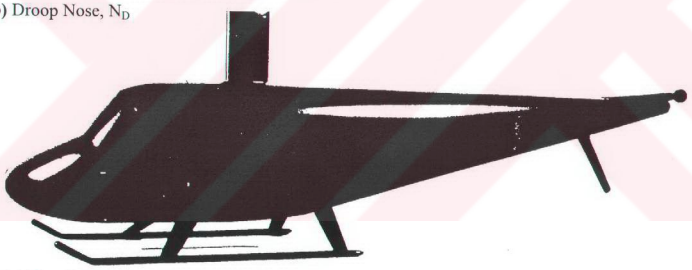

c) Cutback Nose, N_H

Fig. A.3 Models with Full High, Straight Tail Boom T_H

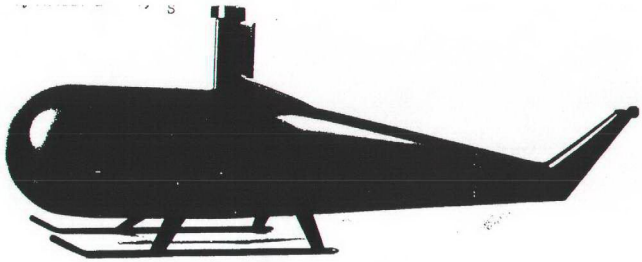

a) Symmetrical Nose, N_S

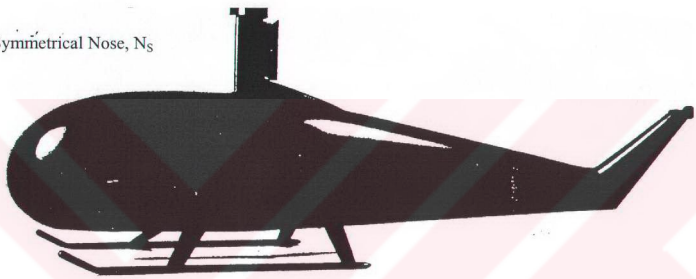

b) Droop Nose, N_D

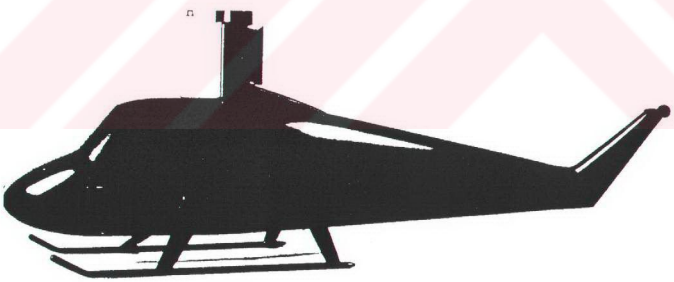

c) Cutback Nose, N_H

Fig. A.4 Models with Full Low, Cranked Tail Boom T_L

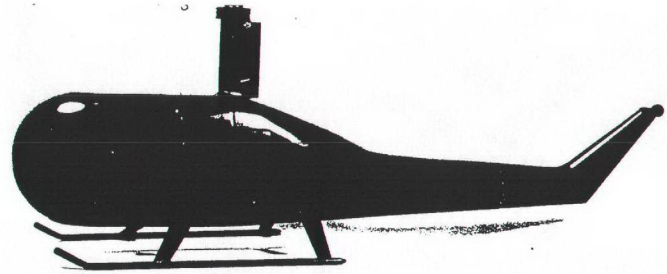

a) Symmetrical Nose, N_S

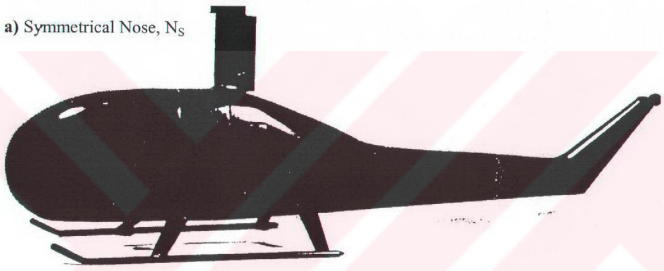

b) Droop Nose, N_D

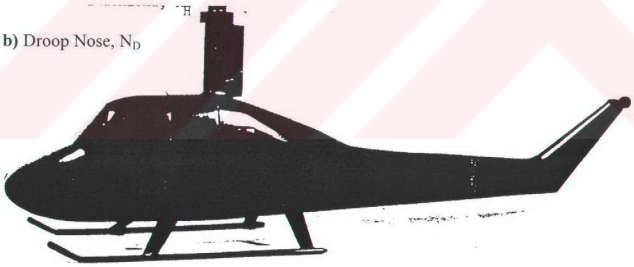

c) Cutback Nose, N_H

Fig. A.5 Models with Full Low, Cranked Tail Boom T_C

APPENDIX B. CALIBRATION DATA OF TEM BALANCE

Table B.1 Rolling Moment Calibration

Roll (LSB)	Pitch (LSB)	Drag (LSB)	Side (LSB)	Lift (LSB)	Yaw (LSB)	moment
-9.31	-0.03	-0.09	0.31	3.27	0.03	-0.0025
-26.31	-0.07	-0.19	0.34	1.84	1.59	-0.0075
-43.39	-0.11	-0.3	0.27	6.24	0.57	-0.0125
-68.96	-0.08	-0.39	0.46	7.46	-0.64	-0.02
-86.09	-0.13	-0.52	0.35	8.72	-0.7	-0.025
-128.15	-0.16	-0.71	0.08	11.52	0.27	-0.0375
-170.18	-0.15	-0.79	-0.21	15.84	0.02	-0.05
-212.09	-0.2	-0.9	-0.48	19.45	3.42	-0.0625
-254.53	-0.23	-1.22	-0.45	20.76	2.62	-0.075
-337.35	-0.3	-1.48	-1.18	28.52	3.44	-0.1
-422.55	-0.29	-1.68	-1.63	34.56	2.95	-0.125
-465.3	-0.38	-1.85	-1.62	36.74	4.78	-0.1375
7.92	-0.01	0.04	-0.02	-0.08	-0.01	0.0025
25.74	-0.04	0.05	0.03	1.86	1.54	0.0075
42.14	-0.04	-0.09	-0.41	2.35	-0.15	0.0125
66.69	-0.03	0	-0.37	2.49	0.08	0.02
82.99	-0.04	-0.13	0.13	6.32	-0.21	0.025
123.72	-0.06	-0.29	0.2	7.93	0.37	0.0375
169.88	-0.09	-4.55	-0.56	12.09	2.9	0.05
210.15	-0.08	-4.54	-0.56	14.36	3.7	0.0625
250.56	-0.08	-4.38	-0.69	16.01	2.57	0.075
331.42	-0.11	-4.55	-0.08	22.84	1.56	0.1
414.37	-0.12	-4.69	0.19	24.5	0.86	0.125
454.86	-0.12	-4.94	0.33	26.94	1.68	0.1375

Table B.2 Pitching Moment Calibration

Roll(LSB)	Pitch (LSB)	Drag(LSB)	Side(LSB)	Lift(LSB)	Yaw(LSB)	moment
-0.14	-3.05	-0.04	-0.05	1.52	0.02	-0.0018
0.17	-8.99	0.03	-0.05	1	0.21	-0.0054
0.81	-14.86	-0.06	-0.16	3.82	-0.1	-0.009
0.1	-23.54	-0.07	-0.92	4.34	-0.01	-0.0144
-0.38	-29.36	0.1	-1.73	6.75	-0.87	-0.018
-0.35	-35.31	0.04	-0.42	7.57	0.52	-0.0216
-0.13	-44.23	-0.14	-0.31	10.83	0.24	-0.027
-0.41	-38.29	-0.08	0.19	9.03	0.91	-0.0324
-0.31	-58.88	-0.23	-0.43	13.85	1.69	-0.036
-0.85	-73.66	-0.61	-0.56	16.14	1.84	-0.045
-0.84	-88.25	-0.6	-1	19.96	1.92	-0.054
-1.33	-103.04	-0.79	-2.24	22.68	2.49	-0.063
-1.99	-117.66	-0.96	-1.98	25.44	3.07	-0.072
-1.88	-132.47	-1.09	-2.14	29.28	4.11	-0.081
-3.53	-147.87	-1.34	-2.95	31.44	2.56	-0.09
-3.86	-221.11	-2.02	-3.64	48.34	6.7	-0.135
-6.03	-294.63	-2.76	-4.39	64.55	8.3	-0.18
-7.64	-441.47	-4.64	-5.61	96.44	13.38	-0.27
-12.09	-589.01	-6.04	-7.54	128.82	18.34	-0.36

Table B.3 Drag Calibration

Roll(LSB)	Pitch(LSB)	Drag(LSB)	Side(LSB)	Lift(LSB)	Yaw(LSB)	Force
0.039	-0.011	2.876	-0.173	0.967	0.009	0.01
0.1	-0.03	15.15	-0.34	1	-0.07	0.03
0.17	-0.05	27.54	-1.14	1.08	-0.32	0.05
0.16	-0.08	35.19	-1.08	1.03	-0.37	0.08
0.26	-0.07	41.62	-1.61	0.7	-0.76	0.1
0.58	-0.08	65.53	-2.04	1.55	-0.83	0.15
0.71	-0.15	88.23	-2.3	1.3	-1.4	0.2
0.91	-0.17	108.7	-3.62	1.61	-1.81	0.25
1.01	-0.19	131.44	-3.73	2.29	-2.73	0.3
1.16	-0.25	150.44	-4.11	2.06	-3.31	0.35
1.53	-0.23	173.56	-4.7	2.81	-4.74	0.4
1.67	-0.27	194.31	-5.04	2.85	-5.66	0.45
1.89	-0.3	219.1	-5.71	2.98	-9.71	0.5
3.17	-0.5	327.01	-8.33	3.22	-12.46	0.75
4.7	-0.83	436.38	-11.06	5.52	-18.1	1
7.72	-1.28	668.03	-17.36	9.49	-31.52	1.5
10.02	-1.87	897.95	-23.49	10.22	-41.82	2

Table B.4 Side-force Calibration

Roll(LSB)	Pitch(LSB)	Drag(LSB)	Side(LSB)	Lift(LSB)	Yaw(LSB)	Force
-0.17	-0.02	0.08	2.72	-0.34	0	0.01
-0.71	-0.09	0.18	7.92	-0.99	-0.75	0.03
-0.92	-0.05	0.56	17.03	-0.6	-0.73	0.05
-1.11	-0.11	0.88	25.67	1.11	-0.72	0.1
-0.17	-0.02	0.08	2.72	-0.34	0	0.15
-2.5	-0.11	1.41	62.19	1.41	-2.15	0.2
-3.37	-0.11	2.13	86.9	2.22	-2.22	0.25
-3.72	-0.11	2.31	97.12	2.37	-2.25	0.3
-4.11	-0.09	2.75	110.7	4.33	-2.26	0.35
-4.73	-0.1	3.26	133.27	5.22	-2.34	0.4
-5.23	-0.12	3.63	146.88	5.39	-2.39	0.45
-5.58	-0.11	3.95	160.56	6.76	-2.9	0.5
-8.59	-0.02	6.52	246.74	8.68	-3.91	0.75
-12.16	-0.01	9.26	340.62	10.85	-7.81	1
-17.86	0.12	14.32	515.1	16.61	-15.67	1.5
-23.64	0.23	20.41	681.52	21.48	-25.81	2
0.04	-0.02	0.04	-3.32	-0.2	-0.01	-0.01
0.15	-0.05	0.23	-10.32	-0.37	0.01	-0.03
0.34	-0.14	0.42	-17.78	-0.55	-0.02	-0.05
0.57	-0.11	1.08	-34.05	-1.01	0.07	-0.1
1.19	-0.18	1.7	-50.74	-0.54	0.16	-0.15
2	-0.18	2.38	-67.83	-0.24	2.29	-0.2
2.27	-0.23	2.74	-81.4	-0.27	2.28	-0.25
2.49	-0.2	3.2	-93.34	-0.69	2.33	-0.3
3.11	-0.27	4.11	-114.95	-1.02	2.44	-0.35
3.55	-0.24	4.72	-126.17	-1.08	5.22	-0.4
4.25	-0.3	5.2	-147.25	-1.3	5.21	-0.45
4.76	-0.31	6.12	-162.27	-0.94	3.06	-0.5
7.53	-0.35	8.82	-238.64	-2.06	8.29	-0.75
10.22	-0.36	12.24	-329.48	-3.79	11.88	-1
15.83	-0.53	18.46	-497.12	-5.59	16.01	-1.5
21.54	-0.61	25.17	-663.99	-8.78	23.7	-2

Table B.5 Lift Calibration

Roll (LSB)	Pitch (LSB)	Drag (LSB)	Side (LSB)	Lift (LSB)	Yaw(LSB)	(Force)
0.19	-0.05	0.04	-0.15	1.95	0.02	0.01
0	-0.07	0.01	-0.75	1.93	0.01	0.02
-0.21	-0.03	0.05	-0.02	2.4	-1.47	0.03
-0.35	-0.1	0.01	-0.78	3.73	-1.43	0.05
-0.37	-0.09	0.05	1.04	5.42	-1.42	0.07
-0.49	-0.19	-0.2	1.24	6.36	-1.45	0.08
-0.95	-0.18	-0.32	1.03	6.72	-1.42	0.1
-0.89	-0.24	-0.33	0.83	8.9	-1.43	0.11
-1.32	-0.28	-0.32	0.66	8.04	-1.45	0.12
-1	-0.24	-0.32	-0.23	10.76	-1.41	0.13
-1.36	-0.21	-0.33	1.14	11.64	-1.45	0.15
-1.27	-0.29	-0.31	0.79	13.45	-1.35	0.17
-1.53	-0.35	-0.54	0.77	15.14	-1.37	0.2
-1.92	-0.38	-0.65	0.41	18.77	-1.31	0.25
-2.26	-0.42	-0.81	0.24	21.84	-1.3	0.3
-2.51	-0.48	-0.96	-0.33	24.43	-1.3	0.35
-2.8	-0.45	-1.03	0.5	27.79	-0.89	0.4
-3.23	-0.46	-0.99	0.55	31.14	-0.84	0.45
-3.35	-0.55	-1.29	-0.1	34.75	-0.85	0.5
-5.01	-0.45	-1.59	-1.09	50.01	-0.65	0.75
-6.76	-0.45	-2.34	-2.3	66.18	-0.06	1
-9.23	-0.5	-3.46	-2.71	98.16	2.51	1.5

Table B.6 Yawing Moment Calibration

Roll(LSB)	Pitch(LSB)	Drag(LSB)	Side(LSB)	Lift(LSB)	Yaw(LSB)	(moment)
0.18	0	7.99	-0.43	0.36	16.94	0.005
0.09	-0.04	11.88	-0.48	-4.09	24.99	0.0075
0.41	-0.11	21.75	-1.2	-0.13	46.38	0.0125
0.13	-0.14	28.81	-1.57	-0.51	57.52	0.0175
0.4	-0.1	45.21	-2.5	-0.09	90.62	0.025
0.57	-0.26	64.69	-3.75	-0.18	131.07	0.0375
-2.84	-0.25	92.84	-5.08	-0.75	192.09	0.05
-2.24	-0.35	113.22	-6.3	0.14	234.92	0.0625
-2.1	-0.34	136.06	-7.71	-0.01	279.96	0.075
-2.13	-0.42	150.52	-8.23	-0.08	312.88	0.0875
-1.59	-0.45	172.15	-9.16	-0.22	351.65	0.1
-0.74	-0.58	230.92	-12.8	-0.43	477.62	0.125
1.4	-0.49	340.3	-20.07	0.37	700.15	0.1875
3.34	-0.53	457.41	-27.88	-2.14	946.77	0.25
9.92	-0.82	677.49	-43.1	-4.4	1413.47	0.375
-0.23	-0.03	8.53	0.12	-1.12	-17.67	-0.005
-0.41	-0.03	11.45	0.23	-1.3	-22.16	-0.0125
-0.16	-0.15	30.22	0.01	-2.39	-66.47	-0.0175
0.02	-0.23	45.91	-0.03	-0.34	-107.6	-0.025
0	-0.29	59.9	-0.1	-2.1	-137.81	-0.0375
0.41	-0.3	78.77	-0.15	-0.89	-179.44	-0.05
0.39	-0.31	109.86	-0.14	-0.73	-253.67	-0.0625
0.39	-0.41	120.97	-0.15	-2.05	-277.6	-0.075
0.73	-0.41	140.64	-0.06	-3.85	-321.58	-0.0875
0.73	-0.43	162.37	-0.1	-1.64	-369.49	-0.1
0.93	-0.44	184.76	-0.29	-1.43	-422.79	-0.1125
1.08	-0.51	208.37	-0.52	-2.85	-475.73	-0.125
1.86	-0.64	314.07	-1.3	-3.99	-720.22	-0.1875
2.69	-0.94	425.12	-2.35	-4.53	-982.06	-0.25
5.04	-1.42	644.31	-4.31	-1.6	-1494.21	-0.375

APPENDIX C. LOCATION AND GEOMETRY OF HORIZONTAL STABILIZERS

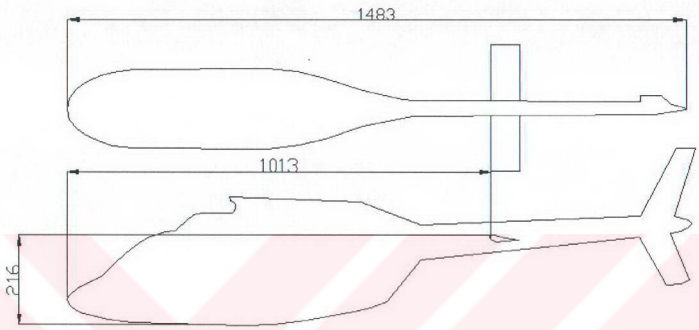

Fig. C.1 Location horizontal stabilizer oh N_HT_F configuration model

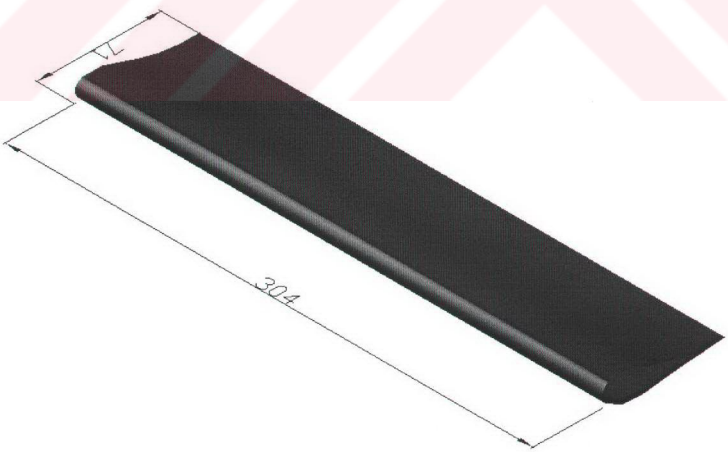

Fig. C.2 Geometry of horizontal stabilizer of N_HT_F configuration model

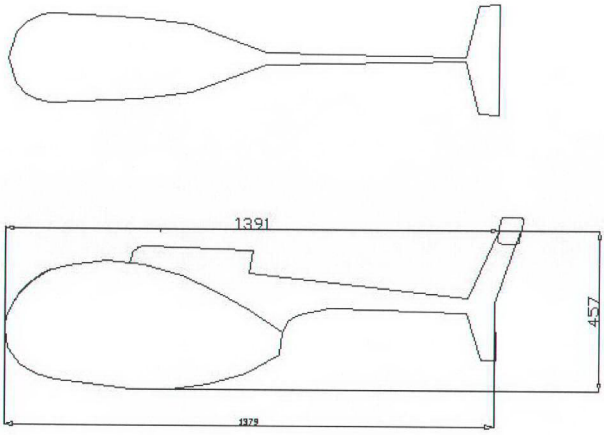

Fig. C.3 Location horizontal stabilizer oh N_DT_E configuration model

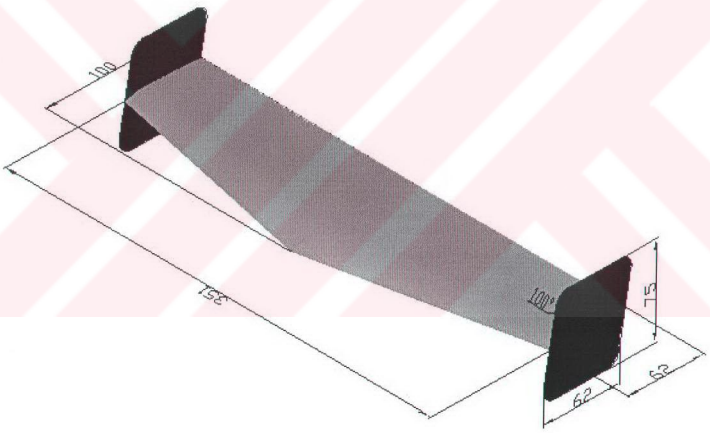

Fig. C.4 Geometry of horizontal stabilizer of N_DT_E configuration model

RESUME

He was born in 1979 in İstanbul. He has finished his primary school in İzmir, he started his high school education in İzmir Karşıyaka Anadolu Lisesi. He has graduated from this school in 1997. In the same year, he started his education in İstanbul Technical University Aeronautical Engineering Department. He has graduated from here in 2001 and started his master's degree education and working as research assistant in the same faculty.